Phase-field modeling of planar interface electrodeposition in lithium-metal batteries

Marcos Exequiel Arguello[a,b,*], Monica Gumulya[c], Jos Derksen[b], Ranjeet Utikar[a], Victor Manuel Calo[d]

[a] WA School of Mines, Mineral, Energy and Chemical Engineering, Curtin University, PO BOX U1987, Perth, WA 6845, Australia.

[b] School of Engineering, University of Aberdeen, Elphinstone Road, AB24 3UE Aberdeen, United Kingdom.

[c] Occupation, Environment and Safety, School of Population Health, Curtin University, PO Box U1987, Perth, WA 6845, Australia.

[d] School of Electrical Engineering, Computing and Mathematical Sciences, Curtin University, PO BOX U1987, Perth, WA 6845, Australia.

_____

Abstract

This paper presents a detailed description of phase-field models of electrodeposition in lithium-anode batteries, along with underlying assumptions and parameters commonly employed. We simulate the coupled electrochemical interactions during a battery charge cycle using finite elements on open-source packages, allowing for parallel computation and time step adaptivity. We compare conventional free energy and grand canonical formulations. We obtain agreement between 1D phase-field simulations and the theoretical Faradic reaction kinetics. We study the mesh-induced errors through spatial convergence analysis. These simulations results set the groundwork for 2D and 3D simulations of dendritic metal electrodeposition in batteries.

Keywords: Phase-field modeling, Electrodeposition, Li-metal battery, Finite element method, Interface thickness

_____

*Corresponding author at: WA School of Mines, Mineral, Energy and Chemical Engineering, Curtin University, PO BOX U1987, Perth, WA 6845, Australia.

Email addresses: m.arguello@postgrad.curtin.edu.au (M.E. Arguello), m.gumulya@curtin.edu.au (M. Gumulya), jderksen@abdn.ac.uk (J. Derksen), r.utikar@curtin.edu.au (R. Utikar), victor.calo@curtin.edu.au (V.M. Calo).

Symbol List

Symbol	Description	Units	Symbol	Description	Units
M	Metal atom specie	[−]	$\tilde{c}$	Normalized Li-metal concentration	[−]
M^+	Cation specie	[−]	$\tilde{c}_+$	Normalized Li-ion concentration	[−]
A^-	Anion specie	[−]	$\tilde{c}_-$	Normalized anion concentration	[−]
C	Li-metal concentration	[mol/m^3]	μ_i^Θ	Chemical potential specie "i" at ref. state	[J/mol]
C_+	Li-ion concentration	[mol/m^3]	ξ	Phase-field order parameter	[−]
C_-	Anion concentration	[mol/m^3]	$g(\xi)$	Double-well function	[J/m^3]
ϕ	Electric potential	[V]	W	Barrier height	[J/m^3]
$\Delta\phi^{eq}$	Interfacial voltage at equilibrium	[V]	δ_{PF}	Phase-field diffuse interface thickness	[m]
$\Delta\phi$	Electric potential difference	[V]	δ_t	Computed phase-field interfacial thickness	[m]
E^Θ	Standard half-cell potential	[V]	γ	Surface Energy	[J/m^2]
$\bar{\mu}$	Electrochemical potential	[J/mol]	L_η	Kinetic coefficient	[1/s]
μ	Chemical potential	[J/mol]	$h_P(\xi)$	Polynomial interpolation function	[−]
η	Total overpotential	[V]	$h_s(\xi)$	Sigmoid interpolation function	[−]
η_a	Activation overpotential	[V]	L_σ	Interfacial mobility	[m^3/(J s)]
η_c	Concentration overpotential	[V]	$\vec{J}$	Flux of lithium species	[mol/(m^{2}s)]
a_i	Activity of specie "i"	[−]	$\vec{J}_+$	Flux of Li-ion species	[mol/(m^{2}s)]
i	Current density	[A/m^2]	D^{eff}	Effective diffusivity	[m^2/s]
i_0	Exchange current density	[A/m^2]	D^s	Diffusivity electrode	[m^2/s]
α	Charge transfer coefficient	[−]	D^l	Diffusivity electrolyte	[m^2/s]
T	Temperature	[K]	Ω	Grand free energy functional	[J]

Symbol	Description	Unit	Symbol	Description	Unit
R	Gas constant	[J/(mol K)]	ϵ^s	Difference chemical potential "s" phase	[J/mol]
n	Valence	[$-$]	ϵ^l	Difference chemical potential "l" phase	[J/mol]
$\mathcal{F}$	Faraday constant	[sA/mol]	χ	Susceptibility factor	[mol^2/(J m^3)]
v	Lithium electrodeposition rate	[m/s]	$\vec{E}$	Electric field vector	[V/m]
λ	Electrodeposited film thickness	[m]	$\vec{\imath}$	Current density vector	[A/m^2]
t	Time	[s]	σ^{eff}	Effective conductivity	[S/m]
s	Solid electrode phase	[$-$]	σ^s	Conductivity electrode	[S/m]
l	Liquid electrolyte phase	[$-$]	σ^l	Conductivity electrolyte	[S/m]
F	Gibbs free energy	[J]	l_x	Battery cell size	[m]
f_{ch}	Helmholtz free energy density	[J/m^3]	l_0	Anode initial thickness	[m]
f_{grad}	Surface energy density	[J/m^3]	ϕ_b	Charging voltage	[V]
f_{elec}	Electrostatic energy density	[J/m^3]	h_0	Length normalization constant	[m]
F_{mix}	Free energy of mixing	[J]	t_0	Time normalization constant	[s]
κ	Gradient energy coefficient	[J/m]	E_0	Energy density normalization constant	[J/m^3]
ρ_e	Charge density	[J/(m^{3}V)]	l_t	Phase-field interface position	[m]
C_m^s	Site density electrode	[mol/m^3]	i_t	Theoretical current density	[A/m^2]
C_m^l	Site density electrolyte	[mol/m^3]	h	Mesh size	[m]
C_0	Bulk Li-ion concentration	[mol/m^3]	h_{min}	Minimum mesh size	[m]
			ε	Electrode position error	[%]

1. Introduction

Our society's continually increasing energy needs have triggered the development of improved energy storage systems. Conventional lithium-ion batteries have dominated the rechargeable battery market since the late 1990s. Unfortunately, these batteries are approaching their performance limit of 250 Wh/kg [1],[2]. Novel chemistry and designs, such as metal anode batteries, are under active research to achieve an energy density of 500 Wh/kg and manufacturing costs lower than $100/kWh [3].

Presently, metallic lithium (Li) is the most prominent anode material for pursuing high energy-density batteries due to its superior theoretical capacity (3860 mAh/g) as well as low reduction potential (-3.04 V vs. standard hydrogen electrode). However, two unresolved challenges remain in the path towards the commercial implementation of lithium metal batteries (LMBs) and lithium anodes in general. Firstly, the formation of inert solid electrolyte interphase (SEI) on the surface of lithium deposits during the recharge cycle, caused by the high reactivity of Li with the electrolyte and subsequent continual consumption, resulting in low Coulombic efficiency (excess of Li, up to 300%, was used in the past for this issue [1]).

The unstable deposition of Li causes the second challenge during the charge cycle, which often occurs in a random and disordered way, leading to the formation of dendrites [4]. This problem compounds with the increase in the lithium reactive area, which enlarges the SEI surface area [5]. Further, lithium dendrites can break due to internal stresses and disconnect from the anode, generating a "dead lithium" compound that does not participate in the electrochemical reaction, further reducing Coulombic efficiency [6]. In the worst-case scenario, the dendrites can pierce the separator and contact the cathode leading to an internal short-circuit and potential thermal runaway of the battery [7],[8]. Rosso et al. [9] reported a fuse effect of the first lithium dendrite reaching the opposite electrode, which melts due to high current density; before the significant front of dendrites eventually connects the cathode and short-circuit the battery (producing an erratic potential).

Developing a stable rechargeable lithium metal anode has become critical for realizing new generation high energy density rechargeable technologies, such as Li-air, Li-S, and Li-flow batteries [10],[11]. The fundamental role of dendrites in electrodeposition processes has motivated several efforts to control the dendritic patterns and make metal-anode batteries commercially viable.

Various computational models seek to understand better the mechanisms of dendrite formation and growth in lithium anodes. Typically, we classify these models into two main groups: thermodynamic and dynamic [12],[13]. Within the dynamic models, phase-field (diffuse-interface) models can simulate the morphology evolution of Li electrodeposit due to reaction-driven phase transformation

within metal anode batteries and rationalize morphology patterns of dendrites observed experimentally [14]-[29].

The phase-field model tracks boundaries and interfaces implicitly using an auxiliary function (the phase-field order parameter), avoiding the need for large mesh displacements with moving boundary conditions. The evolution of the phase-field variables satisfies local equilibrium [30] and free energy minimization [31], leading to nonlinear partial differential equations (PDE's). These models incorporate interfacial energy, interface kinetics, and curvature-driven phase boundary movement rigorously.

Different phase-field models of electrochemical systems describe the phase-field evolution by the Cahn-Hilliard equation [32],[33], the classical Allen-Cahn equation [34], or a modified non-linear Allen-Cahn reaction model [19]. Thus, while some of these models assume linear kinetics [14]-[16],[21], only applicable in the limit of minor deviations from equilibrium (current densities below the limiting current), others describe the nonlinear relation between the phase transformation rate and the thermodynamic driving force, following either Butler–Volmer [17]-[20],[23] or Marcus reaction kinetics [24]. Furthermore, while the derivation of most of these models uses a free energy functional [20],[23],[25],[27], other models also adopt the grand canonical formulation, exchanging concentration for chemical potential as the natural variable to achieve better numerical stability [24],[26].

Typically, the charging conditions for a lithium battery either fix the applied electric potential or the charging current density. Different sets of boundary conditions (BC's) can represent each charging state through different electrodeposition models. In practice, Dirichlet BCs can effectively represent fixed electric potential charging state [16],[17],[20],[22]; in contrast, Neuman BCs at the lithium cation concentration (electrolyte side) represent fixed charging current density state [23],[24],[26]-[28].

There are several aspects related to the morphology evolution of lithium metal electrodes that remain unsolved. A significant effort seeks to develop two-dimensional models to rationalize three-dimensional dendritic patterns observed experimentally qualitatively. Furthermore, various strategies to suppress Li dendrites' growth and weaken the side reactions exist [24]-[29]. However, clarifying the numerical features behind phase-field models has attracted less interest.

This work uses one-dimensional (flat interface) simulations to study various numerical aspects of an electrodeposition phase-field model, thereby setting the groundwork for 2D and 3D simulations. Our study includes a description of the model's equations and critical parameters. A comparative analysis is performed between simulations using a phase-field model derived from a free energy functional

[23] and the recent grand canonical approach [24],[26]. Our results show how spatial resolution (element size) combined with selected phase-field interface thickness affects the evolution rate of simulated electrodeposits under different applied voltages.

Furthermore, we compare the phase-field simulation results against theoretical Faradic reaction rates, and sharp-interface Butler-Volmer kinetics at different applied voltages, assuming uniform and compact electrodeposited film. Finally, we propose a convergence test to study the impact of different mesh resolutions on the electrode position.

2. Governing equations

We model a battery cell composed of a solid metal anode made of pure lithium and a binary liquid electrolyte [26]. The variables of interest are C, representing the concentration of lithium, and ϕ representing the electric potential. When an electric potential difference ($\Delta\phi$) other than the equilibrium value ($\Delta\phi^{eq}$) is imposed to the system (i.e., charging the battery), the binary electrolyte dissociates in M^+ cation and A^- anion species, being transported to the negative (anode) and positive (cathode) electrodes, respectively; developing an ionic concertation gradient [1]. We describe the overpotential as,

$$\eta = \Delta\phi - \Delta\phi^{eq} \tag{1}$$

where $\Delta\phi^{eq}$ is the electrode-electrolyte interfacial voltage at equilibrium, when the electrode electrochemical potential equals to that of the electrolyte, $\bar{\mu}_{electrode} = \bar{\mu}_{electrolyte}$ as determined by the Nernst equation [19],

$$\Delta\phi^{eq} = E^{\Theta} + \frac{RT}{n\mathcal{F}} \ln \frac{a_{M^{n+}} a_e^n}{a_M} \tag{2}$$

where E^{Θ} is the standard half-cell potential, $a_{M^{n+}}$ is the activity of M^+ ion in the electrolyte, a_e^n the activity of the electrons, and a_M the activity of the lithium atom. R, T, n, and $\mathcal{F}$ represent the gas constant, temperature, valence, and Faraday's constant, respectively. Thus, the total overpotential (1) is the overpotential sum of activation $\eta_a = \Delta\phi - E^{\Theta}$ and concentration $\eta_c = -\frac{RT}{n\mathcal{F}} \ln \frac{a_{M^{n+}} a_e^n}{a_M}$.

As a result of the applied overpotential, Faradic reactions occur, current passes through the electrode-electrolyte interface, a Li$^+$ cation gains an electron and deposits on the anode surface (Li$^+ + e^- \rightarrow$ Li), as Figure 1 sketches.
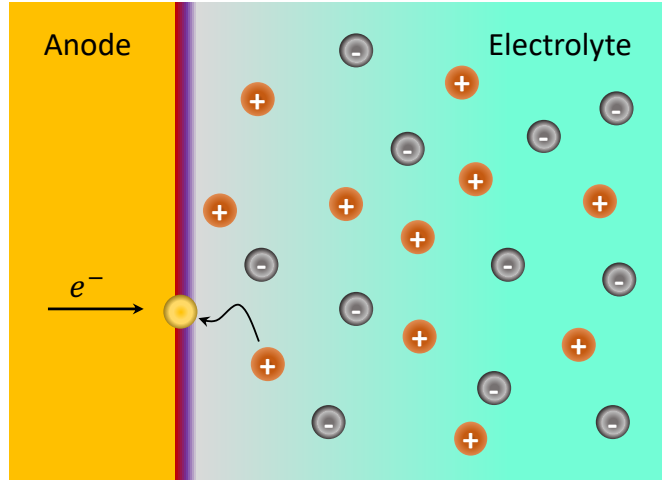
Figure 1 – Schematic of lithium electrodeposition process. Grey, orange, and yellow spheres represent A^- anions, M^+ cations, and M atom, respectively.

The physical processes involved in the electrochemical deposition of lithium are charge and mass transport, where Butler-Volmer kinetics is the standard phenomenological model assumed to govern the charge and mass transport at the electrode-electrolyte interface [35],[36], also known as the current-overpotential equation:

$$i = i_0 \left(e^{-\frac{\alpha n \mathcal{F} \eta}{RT}} - e^{\frac{(1-\alpha)n\mathcal{F}\eta}{RT}} \right)$$ (3)

where i is the current density and i_0 is the exchange current density (assumed constant in this case). The latter parameter is an indicator of the electron-transfer activity on the electrode surface at the equilibrium potential and has been identified as an intrinsic kinetic parameter [29]. The first and second terms in brackets represent the oxidation and reduction reactions, respectively, where α is the charge transfer coefficient that characterizes the symmetry of the forward and reverse reactions [37].

The lithium electrodeposition rate depends on the applied overpotential via a Faradic reaction [38],

$$v = \frac{\partial \lambda}{\partial t} = \frac{i}{\mathcal{F} n C_m^s} = \frac{i_0}{\mathcal{F} n C_m^s} \left(e^{-\frac{\alpha n \mathcal{F} \eta}{RT}} - e^{\frac{(1-\alpha)n\mathcal{F}\eta}{RT}} \right)$$ (4)

where λ represents the electrodeposited film thickness over a time t. C_m^s represents the site density of lithium metal. The superscripts "s" and "l" represent the solid-electrode and liquid-electrolyte phases, respectively. At the mesoscale, the electrode phase is assumed as a pure solid (neglecting any solid phase nanoporosity). Furthermore, this model neglects the presence of a solid-electrolyte interface (SEI), thus neither species nor charge can be stored at the electrode-electrolyte interface.

Phase-field Butler-Volmer equation

Assuming a dilute electrolyte solution, the activity of lithium ions equals its concentration ($a_{M^{n+}} = \tilde{c}_+$), whereby we assume electrons are always available on the surface of the electrode, with an activity equal to unity ($a_e = 1$) [23]; then the equilibrium electrode-electrolyte interfacial voltage (2) is:

$$\Delta\phi^{eq} = E^{\Theta} + \frac{RT}{n\mathcal{F}} \ln \frac{\tilde{c}_+}{a_M} \tag{5}$$

The activity of M-atom (a_M) can be defined variationally by $a_i = e^{\frac{1}{RT}\frac{\delta F_{mix}}{\delta c_i}}$, in terms of the free energy of mixing F_{mix}, see (8) [19], where c_i represents the concentration of specie i.

First, we compute the system's Gibbs free energy, as the summation of the Helmholtz free energy density (f_{ch}), surface energy density (f_{grad}), and electrostatic energy density (f_{elec}), [32],[33],[15]:

$$F = \int_V \left[f_{ch}(C_i) + f_{grad}(\nabla C_i) + f_{elec}(C_i, \phi) \right] dV \tag{6}$$

where C_i represents the chemical species concentrations (e.g., lithium metal atom (C), lithium cation (C_+), and anion (C_-), respectively). The gradient energy density associated with the surface energy of the system is characterised as $f_{grad} = \frac{1}{2}\nabla C_i \cdot \kappa \nabla C_i$, and $f_{elec} = \rho\phi$ is the electrostatic energy density, where $\rho = \sum_i n_i \mathcal{F} C_i$ is the charge density. The Helmholtz free energy density is [19],[23],

$$f_{ch} = W\tilde{c}^2(1-\tilde{c})^2 + C_0 RT\left(\tilde{c}_+ \ln(\tilde{c}_+) + \tilde{c}_- \ln(\tilde{c}_-)\right) + \sum_i c_i \mu_i^{\Theta} \tag{7}$$

with C being normalised against the site density of lithium metal (C_m^S, inverse of molar volume), $\tilde{c} = C/C_m^S$, and ion concentrations, $\tilde{c}_+ = C_+/C_0$ and $\tilde{c}_- = C_-/C_0$, being normalised against the initial bulk concentration of lithium in the electrolyte ($C_0 = c_0 C_m^l$), , where c_0 is the initial bulk lithium molar ratio in the electrolyte, and C_m^l is the site density of the electrolyte phase [23].

The Helmholtz free energy density in (7) shows the contributions of two equilibrium states (solid electrode and liquid electrolyte), the contribution of the lithium ions, and the summation of chemical potentials for each species at a reference state (μ_i^{Θ}). We model the equilibrium states using a double-well function $g(\tilde{c}) = W\tilde{c}^2(1-\tilde{c})^2$, where $W/16$ is the barrier between the two states.

The continuous phase-field variable ξ represents the dimensionless concentration of lithium atom $\tilde{c}$, where $\xi = 1$ and 0 represent the pure electrode and electrolyte phases, respectively; ξ is a non-conserved order parameter in our model [20]. Since the free energy has two local equilibria $\tilde{c}_A$ and $\tilde{c}_B$,

then $\xi = \frac{\tilde{c}-\tilde{c}_A}{\tilde{c}_A-\tilde{c}_B}$ is the phase field with minima at $\xi = 1$ and $\xi = 0$, satisfying the Allen-Cahn reaction

(ACR) model: $\frac{\partial \xi}{\partial t} = \mathcal{R}\left(\frac{\delta F}{\delta c_i}\right)$, a nonlinear generalization of the Allen-Cahn equation for chemical kinetics.

We express, in terms of ξ, the free energy of mixing F_{mix} relative to the standard state as [19]:

$$F_{mix} = f_{ch} + f_{grad} - \sum_i c_i \mu_i^\ominus = \int_V \left[W\xi^2(1-\xi)^2 + C_0 RT\left(\tilde{c}_+ \ln(\tilde{c}_+) + \tilde{c}_- \ln(\tilde{c}_-)\right) + \frac{1}{2}\kappa(\nabla\xi)^2\right]dV \qquad (8)$$

and, following Chen et al. [23], we calculate the activity of M-atom variationally as:

$$a_M = e^{\frac{1}{RT}\frac{\delta F_{mix}}{\delta\xi}} = e^{\frac{g\prime(\xi)-\kappa\nabla^2\xi}{RT c_m^s}} \qquad (9)$$

Substituting (5) and (9) into (1), we obtain the total overpotential expression in terms of ξ:

$$\eta = \Delta\phi - E^\ominus - \frac{RT}{n\mathcal{F}}\left(\ln\tilde{c}_+ - \frac{g'(\xi)-\kappa\nabla^2\xi}{c_m^s RT}\right) \qquad (10)$$

and substituting (10) into the Butler-Volmer (3), we arrive at:

$$i = i_0\left\{e^{-\frac{\alpha n\mathcal{F}}{RT}\left[\eta_a - \frac{RT}{n\mathcal{F}}\left(\ln\tilde{c}_+ - \frac{g'(\xi)-\kappa\nabla^2\xi}{c_m^s RT}\right)\right]} - e^{\frac{(1-\alpha)n\mathcal{F}}{RT}\left[\eta_a - \frac{RT}{n\mathcal{F}}\left(\ln\tilde{c}_+ - \frac{g'(\xi)-\kappa\nabla^2\xi}{c_m^s RT}\right)\right]}\right\} \qquad (11)$$

Finally, we obtain the phase-field evolution equation (Allen-Cahn reaction (ACR) equation) by matching the velocity of the sharp interface limit of the phase-field equation, with the current-overpotential equation as follows [18],[24],[39]:

$$\frac{\partial\xi}{\partial t} = L_\eta\left\{e^{-\frac{\alpha n\mathcal{F}}{RT}\left[\eta_a - \frac{RT}{n\mathcal{F}}\left(\ln\tilde{c}_+ - \frac{g'(\xi)-\kappa\nabla^2\xi}{c_m^s RT}\right)\right]} - e^{\frac{(1-\alpha)n\mathcal{F}}{RT}\left[\eta_a - \frac{RT}{n\mathcal{F}}\left(\ln\tilde{c}_+ - \frac{g'(\xi)-\kappa\nabla^2\xi}{c_m^s RT}\right)\right]}\right\} \qquad (12)$$

where L_η is the electrochemical reaction kinetic coefficient [26]. Figure 2 describes geometrically the phase-field interface position at two different time steps ($t_n < t_{n+1}$), elucidating the relationship between the phase-field time derivative (12) and the lithium electrodeposition rate (4) as:

$$\frac{\partial\xi}{\partial t} = \frac{1}{\delta_{PF}}\frac{\partial\lambda}{\partial t} \qquad (13)$$

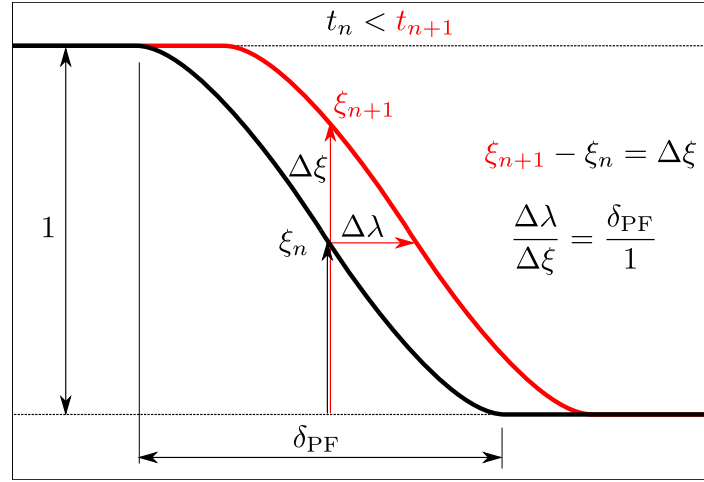where δ_{PF} is the phase-field diffuse interface thickness.

Figure 2 -Diffuse interface geometry. 1D spatial variation of ξ at two moments in time (t_n and t_{n+1})

We relate the Li surface energy (γ) and computed phase-field interfacial thickness (δ_t) to the model parameters according to: $\delta_t = \frac{2\kappa}{3\gamma}$ [40], where $\delta_t \cong \frac{2}{3}\delta_{PF}$, thus $\delta_{PF} \cong \frac{\kappa}{\gamma}$. Now, by comparing (4), (12) and (13), the electrochemical reaction kinetic coefficient becomes

$$L_\eta = \frac{\gamma\, i_0}{\mathcal{F}\, n\, \kappa\, C_m^s} \tag{14}$$

When the system is far from equilibrium, the interface energy driving force is significantly smaller than the electrochemical reaction contribution, Liang et al. [18] linearized the phase-field equation about the interface energy. Using a Taylor expansion, Chen et al. [23] linearized the phase-field Butler-Volmer equation to obtain:

$$\frac{\partial \xi}{\partial t} = -L_\sigma \left[\frac{\partial g(\xi)}{\partial \xi} - \kappa \nabla^2 \xi \right] - L_\eta \frac{\partial h(\xi)}{\partial \xi} \left[e^{\left(\frac{(1-\alpha)n\mathcal{F}\eta_a}{RT} \right)} - \tilde{c}_+ \, e^{\left(\frac{-\alpha n \mathcal{F}\, \eta_a}{RT} \right)} \right] \tag{15}$$

The standard half-cell potential E^Θ is set as 0 for Li/Li$^+$ equilibrium [23], thus our activation overpotential becomes: $\eta_a = \phi$. Moreover, $h(\xi)$ is an interpolation function that smooths the diffuse interface in the current implementation. The interpolation function satisfies $h(0) = 0$, $h(1) = 1$, $\partial h(0)/\partial \xi = \partial h(1)/\partial \xi = 0$, ensuring that $\partial f_{ch}/\partial \xi = 0$ when $\xi = 0$ and $\xi = 1$, for any electric potential value. A popular choice is a polynomial interpolation function $h_P(\xi) = \xi^3(6\xi^2 - 15\xi + 10)$, [41], which satisfies these properties. Herein, we also use a sigmoid interpolation function [42], [43]:

$$h_S(\xi) = \frac{e^{\vartheta\left(\xi - \frac{1}{2}\right)}}{1 + e^{\vartheta\left(\xi - \frac{1}{2}\right)}} \tag{16}$$

where ϑ is a parameter that determines the interface thickness of the interpolation function; we use $\vartheta = 20$, for interpolation between $\xi = 0$ and $\xi = 1$. Figure 3 plots these interpolation functions.
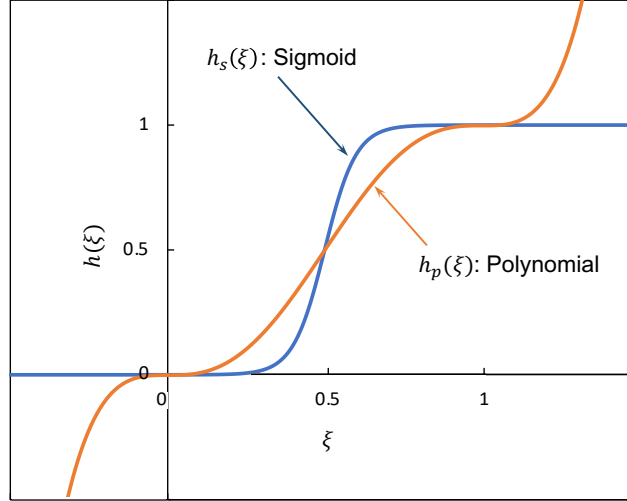
Figure 3 – Comparison between sigmoid vs polynomial interpolation functions

Besides satisfying the above-mentioned properties, the sigmoid function (16) is bound to the range between 0 and 1 for all possible values of ξ. This property is especially useful to deal with numerical overshoots of the phase-field variable ($\xi < 0$ and $\xi > 1$) that are frequent in these simulations. Our experience show that the sigmoid function delivers better the computational efficiency; thus, we use it in all of our simulations.

The interfacial mobility L_σ can be expressed as [23]:

$$L_\sigma = \beta \left\{ \alpha\, e^{-\alpha\left[\frac{n\mathcal{F}\phi}{RT} - \ln \tilde{c}_+\right]} + (1-\alpha)\, e^{(1-\alpha)\left[\frac{n\mathcal{F}\phi}{RT} - \ln \tilde{c}_+\right]} \right\} = \beta \left\{ \alpha\, \frac{\tilde{c}_+^{\alpha}}{e^{\alpha\frac{n\mathcal{F}\phi}{RT}}} + (1-\alpha)\, \frac{e^{(1-\alpha)\frac{n\mathcal{F}\phi}{RT}}}{\tilde{c}_+^{(1-\alpha)}} \right\} \qquad (17)$$

where $\beta = \frac{i_0 \gamma}{RT\mathcal{F}n\kappa C_m^{S\,2}}$. Replacing constant values in (17), Figure 4 plots the exponential variation of L_σ within the range of charging voltages relevant for lithium dendrite electrodeposition ($\phi = 0$ to $-3\ [V]$), and Li-ion concentration ranging $0 \leq \tilde{c}_+ \leq 1$.
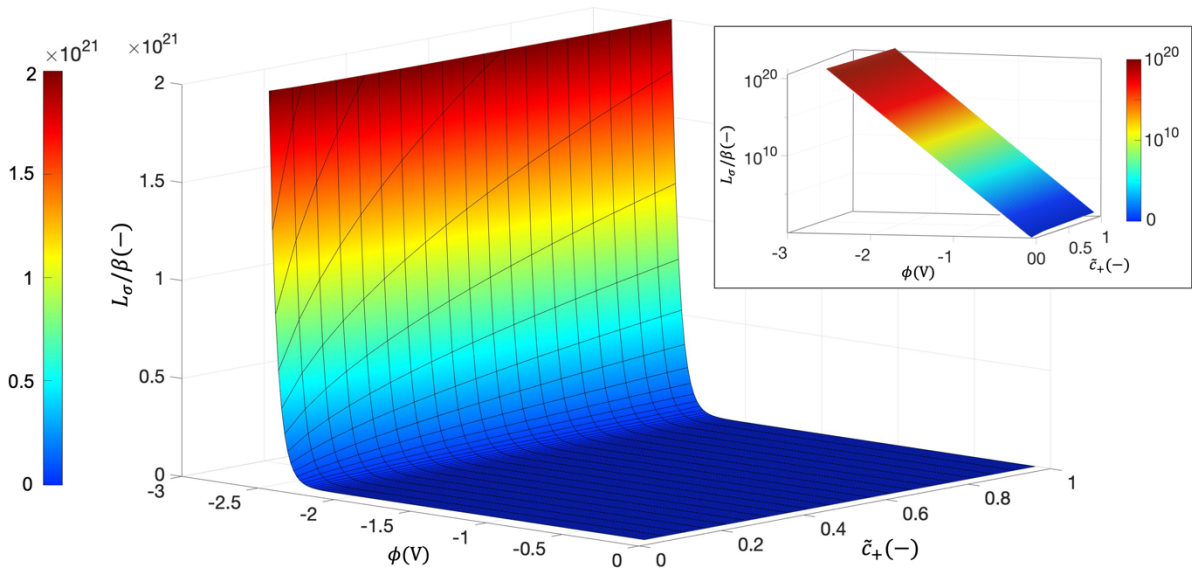
Figure 4 – Interfacial mobility (L_σ/β) value within the range of charging voltages relevant for dendritic electrodeposition of lithium ($\phi = 0$ to -3 $[V]$), and range of Li-ion concentration ($0 \leq \tilde{c}_+ \leq 1$). The inset plots L_σ/β in logarithmic scale for better appreciation.
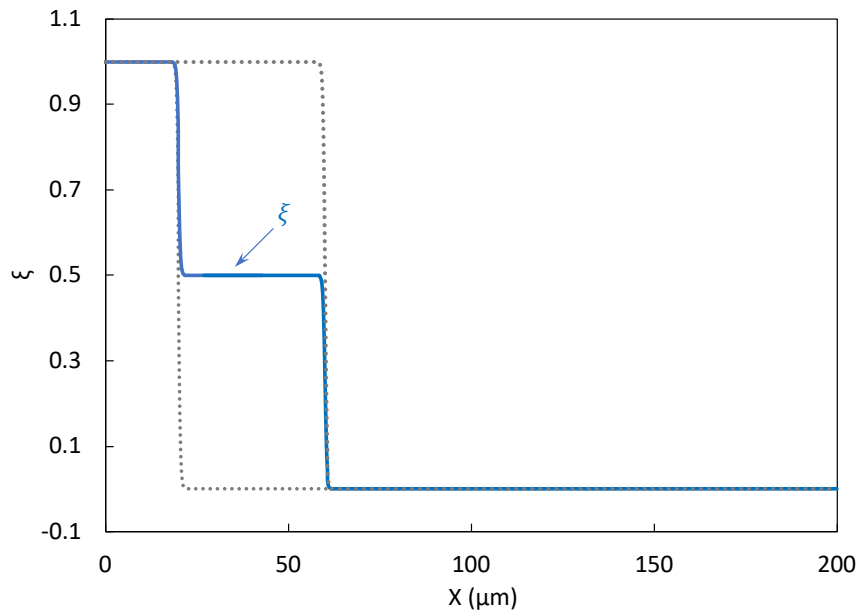

Figure 5 – "Step-like" diffuse interface due to the imbalance between interface energy term (L_σ) and electrochemical reaction contribution. X: direction normal to phase-field interface (see Section 3).

Figure 4 shows that the L_σ value (assumed constant for each simulation) needs to be adjusted to the selected voltage that charges the battery. Furthermore, the L_σ dependency on $\tilde{c}_+$ is lower, but not insignificant. Therefore, selecting an adequate value for L_σ is vital to achieve the right balance

between the phase-field interface energy term and the electrochemical reaction contribution. This adjustment avoids the unphysical broadening of the phase-field interface when simulating larger electro potential values, see Figure 5.

Diffusion migration

A diffusion-migration equation describes the motion of charged chemical species (lithium-ion) in the fluid electrolyte. The temporal evolution of $\tilde{c}_+ = C_+/C_0$, satisfies the modified Nernst-Planck diffusion equation, which describes the flux of Li-ions under the influence of both a concentration gradient (∇C_+) and an electric field ($\nabla \phi$) [44]:

$$\frac{\partial C_+}{\partial t} = -\nabla \cdot \vec{J}_+ \tag{18}$$

where the flux of lithium-ion species is:

$$\vec{J}_+ = -D^{eff} \left(\nabla C_+ + \frac{n\mathcal{F}}{RT} C_+ \nabla \phi \right) \tag{19}$$

Herein, the effective diffusivity is interpolated by $D^{eff}(\xi) = D^s h(\xi) + D^l [1 - h(\xi)]$, where D^s and D^l are the electrode and electrolyte diffusivities respectively.

Alternatively, Plapp [45] demonstrated that exchanging concentration (C) for chemical potential (μ) as one of the dependent variables ensures constant chemical potential at equilibrium; in addition, simulations are more robust at low concentration values. This grand canonical formulation was recently applied to other phase-field models of electrokinetic [24],[26]. The grand free energy functional of an electrochemical system is [24]:

$$\Omega[\xi, \mu, \phi] = \int_V \left[f_{ch}(\xi, \mu) + f_{grad}(\nabla \xi) + f_{elec}(\mu, \phi) \right] dV \tag{20}$$

which represents the grand canonical version of (6). Thus, by making use of the Nernst-Einstein relation ($\nabla C = C\nabla\mu/RT$), the flux equation of all lithium species can be written as follows:

$$\vec{J} = -\frac{D^{eff} C_{Li}}{RT} (\nabla \mu + n\mathcal{F}\nabla\phi) \tag{21}$$

where the concentration of lithium species C_{Li} has the contribution from the electrode and electrolyte phases. However, derivation of diffusion equation by Hong et al. [26] does not consider the effect of lithium-metal diffusivity in the flux of lithium species, by assuming it to be much smaller than the diffusivity of lithium-ion; thus: $\vec{J} \cong -\frac{D^l C_+}{RT} (\nabla \mu + n\mathcal{F}\nabla\phi)$, where the concentration of lithium ion is interpolated in terms of ξ and μ as [46]:

$$C_+(\mu,\xi) = \tilde{c}_+(\mu,\xi)\, C_0 = C_m^l c^l(\mu)[1-h(\xi)] = C_m^l \frac{e^{\left(\frac{\mu-\epsilon^l}{RT}\right)}}{1+e^{\left(\frac{\mu-\epsilon^l}{RT}\right)}}[1-h(\xi)] \tag{22}$$

with $c^l(\mu)$ as the local lithium molar ratio at liquid phase, and $\epsilon^l = \mu^{0l} - \mu^{0N}$ as the difference in the chemical potential of lithium and neutral components at the initial equilibrium state in the liquid phase. The flux assumption creates an inconsistency in the diffusion equation via the grand canonical approach; where the chemical potential of all lithium species (μ) only considers the contribution of the flux of lithium-ion species ($\vec{J}_+$). The grand canonical formulation used this assumption when it was initially derived as a solidification model for phase-field processes [45], and then adapted to model metal electrodeposition [24],[26], where only the charged species are affected by the electric field (ϕ).

Moreover, an additional term ($\frac{C_m^s}{C_0}\frac{\partial\xi}{\partial t}$) needs to be included in the Nernst-Planck diffusion equation, to account for the amount of lithium-ion elimination in the electrolyte solution, due to electrodeposition on the solid phase (metal electrode). Thus, diffusion equation is finally expressed as [44]:

$$\frac{\partial\tilde{c}_+}{\partial t} = \nabla\cdot\left(D^{eff}\,\nabla\tilde{c}_+ + D^{eff}\frac{n\mathcal{F}}{RT}\tilde{c}_+\nabla\phi\right) - \frac{C_m^s}{C_0}\frac{\partial\xi}{\partial t} \tag{23}$$

The diffusion equation in terms of the chemical potential (μ), following Hong et al. [26], becomes:

$$\frac{\partial\mu}{\partial t} = \frac{1}{\chi}\left[\nabla\cdot\frac{D^l\tilde{c}_+}{RT}\frac{C_0}{C_m^l}(\nabla\mu + n\mathcal{F}\nabla\phi) - \frac{\partial h}{\partial t}\left(c^s\frac{C_m^s}{C_m^l} - c^l\right)\right] \tag{24}$$

where the susceptibility factor χ is:

$$\chi = \frac{\partial c^s}{\partial\mu}h\frac{C_m^s}{C_m^l} + \frac{\partial c^l}{\partial\mu}[1-h] \tag{25}$$

Electrostatic Potential

We account for the electrostatic potential distribution ϕ using the charge continuity equation [15]:

$$\frac{\partial\rho}{\partial t} = -\nabla\cdot\vec{\imath} \tag{26}$$

where $\vec{\imath}$ is the current density vector and $\rho = \Sigma_i n_i\mathcal{F}c_i$ is the charge density. Experimental observations support the assumption that space-charge effects do not affect the stability of electrodeposits [47]. Therefore, we ignore the double-layer effects and assume electroneutrality ($\tilde{c}_+ = \tilde{c}_-$, $\mu_+ = \mu_-$) [24]. Thus, electroneutrality means that $\rho^l = 0$ and $\rho^s = -n\mathcal{F}C$, where $C = C_m^s\tilde{c}$; thus, $\Delta\rho$ represents the electrons that create neutral C from C_+ in the electrolyte. Another benefit of

the electroneutrality assumption is the model simplification that only needs to track the lithium cation (Li^+) movement.

Therefore, making use of Ohm's law in the continuity equation, $\vec{\imath} = \sigma \vec{E}$, where σ is the conductivity and $\vec{E} = -\nabla\phi$ is the electric field, we obtain the Poisson equation, including a source term to represent the charge that enters or leaves the system due to the electrochemical reaction:

$$\nabla \cdot \left[\sigma^{eff}(\xi)\,\nabla\phi\right] = n\mathcal{F}C_m^s \frac{\partial \tilde{c}}{\partial t} \tag{27}$$

Since the phase-field variable ξ corresponds to the lithium atom concentration ($\tilde{c}$), we can express the previous equation as [23]:

$$\nabla \cdot \left[\sigma^{eff}(\xi)\,\nabla\phi\right] = n\mathcal{F}C_m^s \frac{\partial \xi}{\partial t} \tag{28}$$

We interpolate the effective conductivity by $\sigma^{eff}(\xi) = \sigma^s h(\xi) + \sigma^l[1 - h(\xi)]$, where σ^s and σ^l are the electrode and electrolyte phase conductivity, respectively.

3. System Layout & Properties

Generally, the computational domain for a battery simulation comprises the anode and cathode regions and the space between the electrodes filled with electrolyte [48]. However, for most phase-field simulations of metal electrodeposition, including those performed herein, the cathode region is reduced into a current collector boundary condition on the electrolyte side of the domain (Figure 6).

We model a battery cell, with a traditional 1D sandwich architecture, and an initial interelectrode distance of $180\mu m$, undergoing a recharging process under fixed applied electric potential status. The initial structure consists of a $20\mu m$-thick metal anode ($l_0 = 20\mu m$), made up of pure lithium, separated from the liquid electrolyte by a smooth interface, as Figure 6 shows. The initial condition drives from the equilibrium solution for a one-dimensional transition zone between solid ($\xi = 1$) and liquid ($\xi = 0$), where our variables ($\xi, \tilde{c}_+, \phi$) vary in the "x" spatial direction normal to the interface according to $\xi(x) = \frac{1}{2}\left[1 - tanh\left(x\sqrt{\frac{W}{2\kappa}}\right)\right]$ [41].
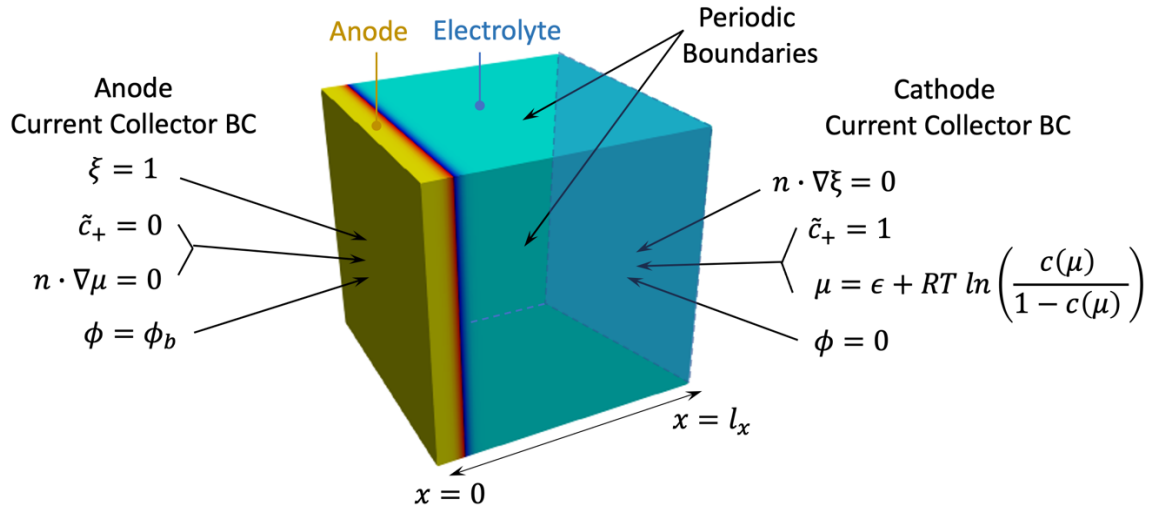
Figure 6 – Boundary conditions for battery charge simulation

On the cell's right side, the electrolyte is 1M $LiPF_6$ dissolved in EC/DMC 1:1 volume ratio solution, including Li^+ cation and PF_6^- anion species. We compute the site density of the electrolyte (C_m^l) using the density (1.3 g/cm^3) and molar mass (90 g/mol) of the electrolyte; similarly, the site density of the electrode C_m^s uses the density (0.534 g/cm^3) and molar mass (6.941 g/mol) of pure lithium [26].

We use a Dirichlet boundary condition $\xi = 1$ on the left boundary for the phase-field order parameter (solid electrode phase) and a non-flux Neumann boundary condition on the right boundary, which allows the electrodeposition process (ξ changing from 0 to 1) when the reaction front approaches the right boundary (cathode).

For the Li-ion concentration, we apply Dirichlet boundary conditions, $\tilde{c}_+ = 0$ and $\tilde{c}_+ = 1$, to the left and right cell boundaries, respectively. Thus, the Li-ion flows into the battery (electrolyte side), ensuring that the amount of Li deposited at electrode-electrolyte interface equals the amount of Li^+ supplied on the electrolyte side, thus avoiding quick Li-ion depletion and keeping the electrodeposition process running for the entire simulation time.

Alternatively, when solving for the chemical potential μ, instead of $\tilde{c}_+$, we apply a non-flux Neumann boundary condition on the left boundary (electrode phase), indicating a constant lithium molar ratio, while we apply a time-varying Dirichlet boundary condition on the electrolyte side (right boundary), allowing for a change on the chemical potential value when the reaction front approaches the right boundary. Table 1 summarizes our set of boundary conditions.

Additionally, Table 2 presents the parameters we use in the current phase-field model. The normalization constants for length, time, energy density and concentration scales are set as $h_0 = 1[\mu m]$, $t_0 = 1[s]$, $E_0 = 2.5 \times 10^6 [\text{J/m}^3]$, and $C_0 = 1 \times 10^3 [mol/m^3]$, respectively.

Table 1 – Boundary Conditions (1D Problem)

	Electrode ($x = 0$)	Electrolyte ($x = l_x$)
Phase - Field	$\xi = 1$	$n \cdot \nabla \xi = 0$
Li-ion Concetration	$\tilde{c}_+ = 0$	$\tilde{c}_+ = 1$
or		
Chemical Potential	$n \cdot \nabla \mu = 0$	$\mu = \epsilon + RT \, ln\left(\dfrac{c(\mu)}{1 - c(\mu)}\right)$
Electrostatic Potential	$\phi = \phi_b [V]$	$\phi = 0 \, [V]$

Table 2 – Simulation Parameters

Variable name	Symbol	Real value	Normalized	Source
Exc. Current Density	i_0	$30[\text{A/m}^2]$	30	[49]
Surface Energy	γ	$0.5[\text{J/m}^2]$	0.22	[50],[51]
Barrier height	W	$W = 12\dfrac{\gamma}{\delta_t} = 6.67 \times 10^6 [\text{J/m}^3]$	2.67	Computed
Gradient energy coeff	κ	$\kappa = \dfrac{3\,\gamma\,\delta_t}{2} = 8.34 \times 10^{-7} [\text{J/m}]$	0.335	Computed
Kinetic coeff	L_η	$L_\eta = i_0 \dfrac{\gamma}{n\,C_m^s\,\mathcal{F}\,\kappa} = 0.00271[1/s]$	0.00271	Computed
Difference in the	ϵ^s	$\epsilon^s = \mu^{0s} - \mu^{0N}$	-13.8	[26]
chemical potential	ϵ^l	$\epsilon^l = \mu^{0l} - \mu^{0N}$	2.631	[26]
Site density electrode	C_m^s	$7.64 \times 10^4 [\text{mol/m}^3]$	76.4	[26]
Site density electrolyte	C_m^l	$1.44 \times 10^4 [\text{mol/m}^3]$	14.4	[23]
Bulk Li-ion Concen.	C_0	$1000[\text{mol/m}^3]$	1	Computed
Conductivity electrode	σ^s	$10^7 [\text{S/m}]$	10^7	[23]
Conductivity electrolyte	σ^l	$1.19[\text{S/m}]$	1.19	[52]
Diffusivity electrode	D^s	$7.5 \times 10^{-13} [\text{m}^2/\text{s}]$	0.75	[23]
Diffusivity electrolyte	D^l	$3.197 \times 10^{-10} [\text{m}^2/\text{s}]$	319.7	[52]

Table 2 shows that although the electrode and electrolyte materials can exhibit Li/Li^+ dependent conductivities and diffusivities, their values are set constant across each phase for simplicity.

4. Numerical Implementation

Our PDE system includes the phase-field (15), diffusion (23) or (24), and electric potential (28) equations. We solve this system using finite elements implemented in the open-source computing platform FEniCS [53],[54].

We use a second-order backward-difference (BDF2) time marching scheme with an adaptive time step size. The BDF2 scheme is an implicit integration method that requires solutions at two previous time steps and can start using the first-order backward-difference method (BDF1). BDF2 has second-order accuracy and dampens unresolved frequencies, unlike the commonly used Crank-Nicolson method. Liao et al. [55] demonstrate numerically the effectiveness of BDF2 time integrator for phase-field crystal model, especially when coupled with an adaptive time-step strategy.

Using standard variational arguments [56],[57], we convert the PDEs into a system of nonlinear equations. We solve the non-linear system using PETSc's Scalable Nonlinear Equations Solvers (SNES), combined with iterative biconjugate gradient stabilized method (BiCGStab) for the linear system [58]. The nonlinear relative convergence tolerance for SNES is $\varepsilon_{rel} = 10^{-7}$.

We improve the performance of the linear solver by using the sigmoid interpolation function (16), reducing by 30% the number of linear iterations, thus reducing the computational cost significantly. We also use the PETSc scalable implementation of parallel ILU preconditioner (hypre_euclid) [58].

Phase-Field Diffuse Interface Thickness & Mesh Size: A Discussion

The interface thickness between the lithium electrode and the electrolyte is about $5nm$ [59]. Simulating this thickness is impractical due to the computational cost [14],[15]; the smaller the interface thickness, the finer the grid resolution (mesh size) used, causing the simulation time to increase significantly. Therefore, broadening the interface for computational reasons (thin interface formulations) is essential in our model [60],[61]. However, the thickness selection must follow reasonable criteria since using an oversized interface deviates the simulation from reality [62].
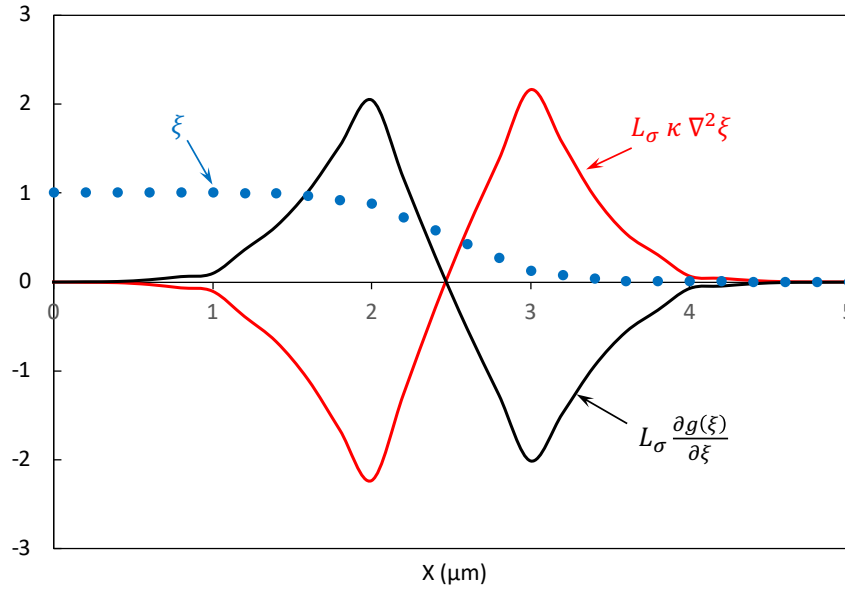
Figure 7 – Schematic of phase-field diffuse interface (●) as a result of the equilibration of the opposing effects of the energy barrier ($\frac{\partial g(\xi)}{\partial \xi}$) and the gradient energy ($\kappa \nabla^2 \xi$).

An analysis of the published data reveals that the interface thickness used in phase-field simulations of electrodeposition are varied (from less than $0.1nm - 1D$ [15] up to $50[\mu m]$ [25]), although this thickness is often not reported [22],[23],[27],[28]; this fact shows the lack of agreement in criteria in the definition of the phase-field interface. In our phase-field model (15), the phase-field diffuse interface thickness (δ_{PF}) results from the interaction between two opposite effects on the interfacial energy term ($\frac{\partial g(\xi)}{\partial \xi} - \kappa \nabla^2 \xi$), as Figure 7 shows. On the one hand, the reduction of the volume of material where ξ is between 0 and 1 (proportional to $W \propto \gamma$), and on the other hand, the diffusion of the interface to minimize the energy relative to the gradient of ξ (proportional to κ). [40],[41]. Two different expressions for W and κ are common in phase-field models of electrokinetics available depending on the definition of phase-field thickness (δ_t). Boettinger et al [41] characterized the characteristic thickness (δ_B) from an equilibrium solution: $\xi(x) = \frac{1}{2}\left[1 - tanh\left(x\sqrt{\frac{W}{2\kappa}}\right)\right]$ (the term multiplying x, $2\delta_B = \sqrt{2\kappa/W}$); alternatively, Cahn-Hilliard [40] used the slope at $x = 0$ to estimate an interface thickness (δ_{CH}). Table 3 summarizes different expressions for W and κ; that relate these phase-field interface thicknesses: $\delta_{CH} = 4\delta_B$.

Table 3- Comparison between different expressions for W and κ in literature [40],[41].

Variable name	Symbol	Cahn-Hilliard	Boettinger et al.
Theoric Interfacial thickness	δ_t	$2\sqrt{2\kappa/W}$	$\sqrt{\kappa/2W}$
Barrier height	W	$12\dfrac{\gamma}{\delta_{CH}}$	$3\dfrac{\gamma}{\delta_B}$
Gradient energy coefficient	κ	$\dfrac{3\,\gamma\,\delta_{CH}}{2}$	$6\gamma\delta_B$

Section 5 further analyses the effect of the phase-field interface thickness on the electrodeposition rate simulation results, which ultimately control the temporal evolution of the electrodeposits. As a default set-up for our simulations, we adopt a phase-field interface thickness of $\delta_{PF} = 1[\mu m]$, with $h = 0.25[\mu m]$ spatial resolution (4 linear elements across the diffuse interface).

5. Results and Discussion

We perform several simulations to evaluate our electrodeposition model and to guide further 2D and 3D battery simulations. These studies compare simulations results using phase-field models derived using a free energy functional [23] against those using a grand canonical approach [24],[26]. We study the effect of the applied overpotential (and the prediction's agreement with Faradic kinetics), as well as we analyze the prediction sensitivity to the phase-field interface thickness. Additionally, we perform a convergence test using different mesh resolutions, and the relative differences of the electrode position is computed for both formulations.

First, we study the spatial variation of the phase-field, Li-ion concentration, and electric potential at the initial stage and two different times (100s and 200s) for a flat interface (one-dimensional simulation) as Figure 8 shows. These results illustrate our set of initial conditions, as well as the evolution of our system's variables ($\xi, \tilde{c}_+, \phi$) by solving three coupled (15), (23), and (28). This model corresponds to a phase-field derivation from a free energy functional. The growth of Li deposit starts when we apply a negative voltage ($\phi_b = -0.45[V]$) to the cell (charging state). We use a phase-field interface thickness of $\delta_{PF} = 1[\mu m]$, with spatial resolution of $h = 0.25[\mu m]$ (mesh size) combined with time step adaptivity [63],[64].
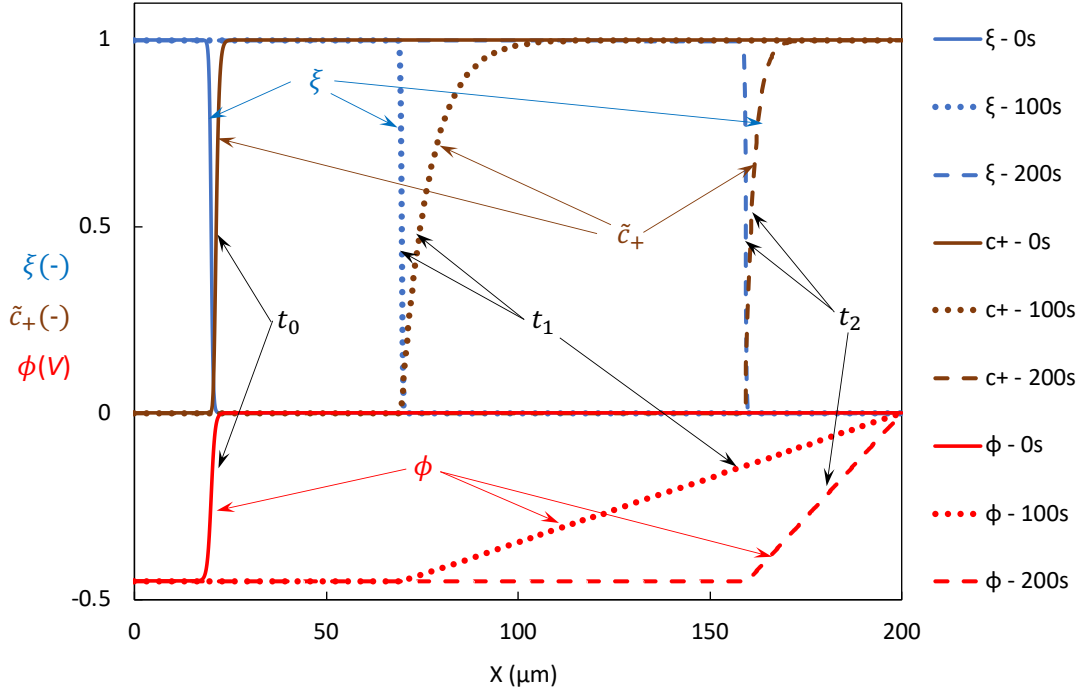
Figure 8 – Spatial variation of phase-field (ξ), Li-ion concentration ($\tilde{c}_+$), and electric potential (ϕ) in electrode-electrolyte system during charging ($\phi_b = -0.45[V]$) at $t_0 = 0\ s$ (solid) , $t_1 = 100\ s$ (dotted), and $t_2 = 200\ s$ (dashed).

Figure 8 shows that the electrode-electrolyte interface moves as lithium deposits on the electrode surface as time progresses. The electrodeposition evolution results in a steeper distribution of Li-ion concentration at the electrode-electrolyte interface (compare the concentration profile at $t_1 = 100\ s$ and $t_2 = 200\ s$), due to the increase of the electric potential gradient (migration forces) as the interelectrode distance shortens. Finally, in agreement with the experimental observations of Nishikawa et al. [38], the electrodeposition velocity increases over time (compare the interface position at $t_1 = 100\ s$ and $t_2 = 200\ s$).

We repeat the simulation switching lithium-ion concentration ($\tilde{c}_+$) for chemical potential (μ) as a dependent variable (grand canonical formulation) [24],[26],[45]. Even though the grand canonical approach was recently applied to other phase-field models of electrokinetics [24],[26], to the best of our knowledge, there is no evidence comparison between the performance of each formulation in this field. Thus, we verify the agreement between simulation results and identify advantages and disadvantages of each approach. Figure 9 shows the initial conditions for the grand canonical approach, as well as the evolution of our system's variables (ξ, μ, ϕ) by solving three coupled equations. Again, we apply a negative voltage ($\phi_b = -0.45[V]$) to the cell (charging state). These results show a distribution of field variables similar to that of the free energy approach.
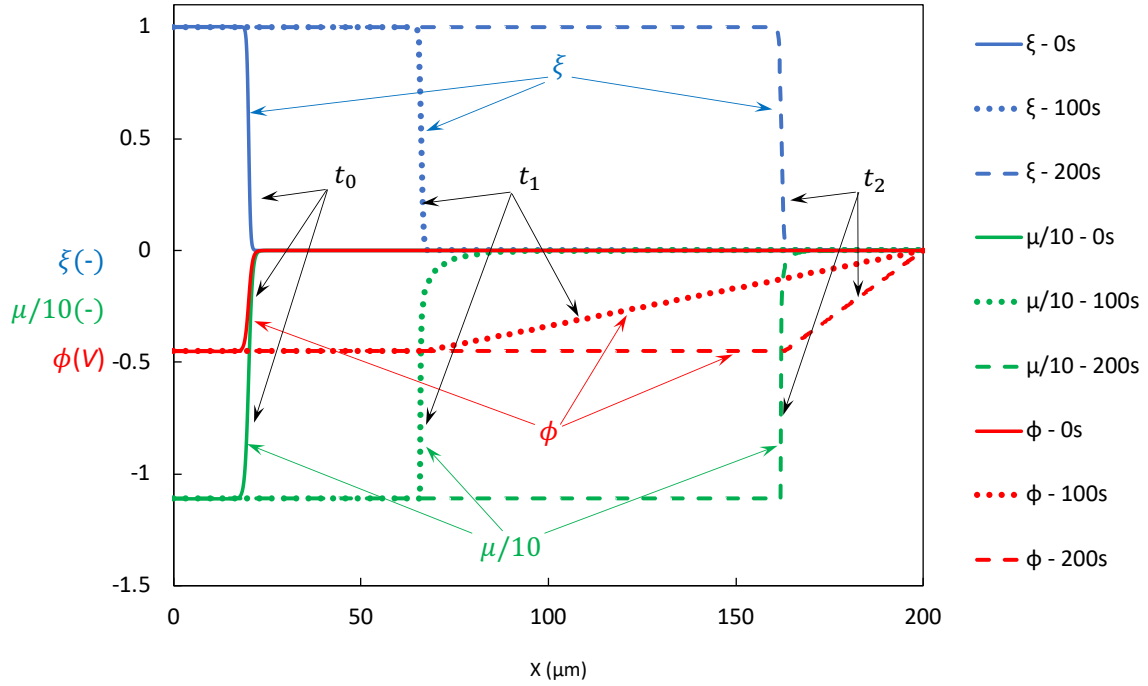
Figure 9 – Spatial variation of phase-field (ξ), chemical potential (μ) and electric potential (ϕ) in electrode-electrolyte system during charging ($\phi_b = -0.45[V]$) at $t_0 = 0\ s$ (solid), $t_1 = 100\ s$ (dotted), and $t_2 = 200\ s$ (dashed).
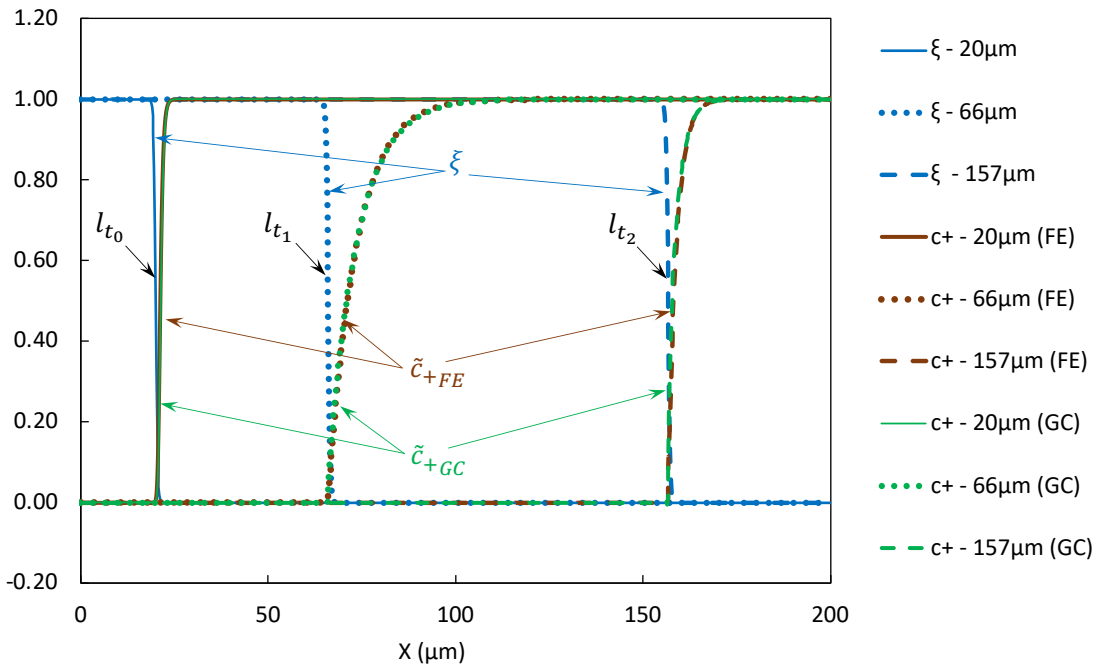

Figure 10 –lithium-ion concentration ($\tilde{c}_+$) comparison between free energy (FE) and grand canonical (GC) approaches using sigmoid smoothing (29). Phase field (ξ) (blue) for reference; Charge: $\phi_b = -0.45[V]$; $l_{t_0} = 20\ \mu m$ (solid), $l_{t_1} = 66\ \mu m$ (dotted), and $l_{t_2} = 157\ \mu m$ (dashed).

Furthermore, Figure 10 shows the agreement between the lithium-ion concentration ($\tilde{c}_+$) at different phase-field interface positions (l_t), using the free energy formulation and the grand canonical approach when using sigmoid smoothing [45]:

$$\tilde{c}_+(\mu, \xi) = \frac{C_m^l}{C_0} e^{\left(\frac{\mu - \epsilon^l}{RT}\right)} \left[1 + e^{\left(\frac{\mu - \epsilon^l}{RT}\right)}\right]^{-1} \tag{29}$$

Figure 10 shows a steeper Li^+ concentration distribution as the front approaches the opposite electrode ($l_{t_2} > l_{t_1}$); since proximity induces a higher electric potential gradient ($\nabla\phi$) as the model approaches the battery short-circuit condition. This produces an increase of the Li^+ concentration at the electrode-electrolyte interface ($\xi = 0.5$), from $\tilde{c}_+ = 0.03$ at $l_{t_1} = 66[\mu m]$, to $\tilde{c}_+ = 0.06$ at $l_{t_2} = 157[\mu m]$, leading to faster rates of lithium electrodeposition according to (15).

We compare the electrodeposition rates predicted by the free energy ($\tilde{c}_+$) and grand canonical (μ) approaches under different applied voltages. Figure 11 displays the electrodeposit position ($\xi = 0.5$) over time for different applied voltages ($\phi_b = -0.45, -0.60, -0.75[V]$).

We also compare the phase-field results against the theoretical Faradic model, used to theoretically interpret the growth rate of a uniform deposited film [38],[65]. The theoretical operating current density across the flat electrode surface is $i_t = \phi_b / \left(\frac{l_t}{\sigma^s} + \frac{l_x - l_t}{\sigma^l}\right)$, where ϕ_b, σ^s, σ^l, l_x and l_t, are the applied voltage, electrode and electrolyte conductivities, battery cell size, and the electrode surface position at time t, respectively. Therefore, we compute the theoretical electrodeposited film thickness, $\lambda = l_t - l_0$, integrating Faraday's law (4) over time as follows:

$$\lambda = \frac{\int_0^t i_t dt}{n\mathcal{F}C_m^s} \tag{30}$$

In (30), we define a set of electrode positions $\left\{l_{t_i} \in \mathbb{R} \ s.t. \ l_0 \leq l_{t_i} \leq l_x\right\}$, using a small interval size between these positions (i.e., $\Delta l_t = 0.01[\mu m]$ achieves convergence). We calculate the theoretical current density $i_{t_i}(l_{t_i})$ for each position, and estimate the Faradic electrodeposition rate, $v(t_{n+1})$, using the forward Euler method:

$$v(t_{n+1}) = \frac{\lambda(t_{n+1}) - \lambda(t_n)}{t_{n+1} - t_n} = \frac{l_t(t_{n+1}) - l_t(t_n)}{t_{n+1} - t_n} \tag{31}$$

Thus, solving for t_{n+1} from (31), we obtain a set of $t_i \ vs \ l_{t_i}$ values that allows for comparison with phase-field model predictions within a range of charging voltages as Figure 11 shows.
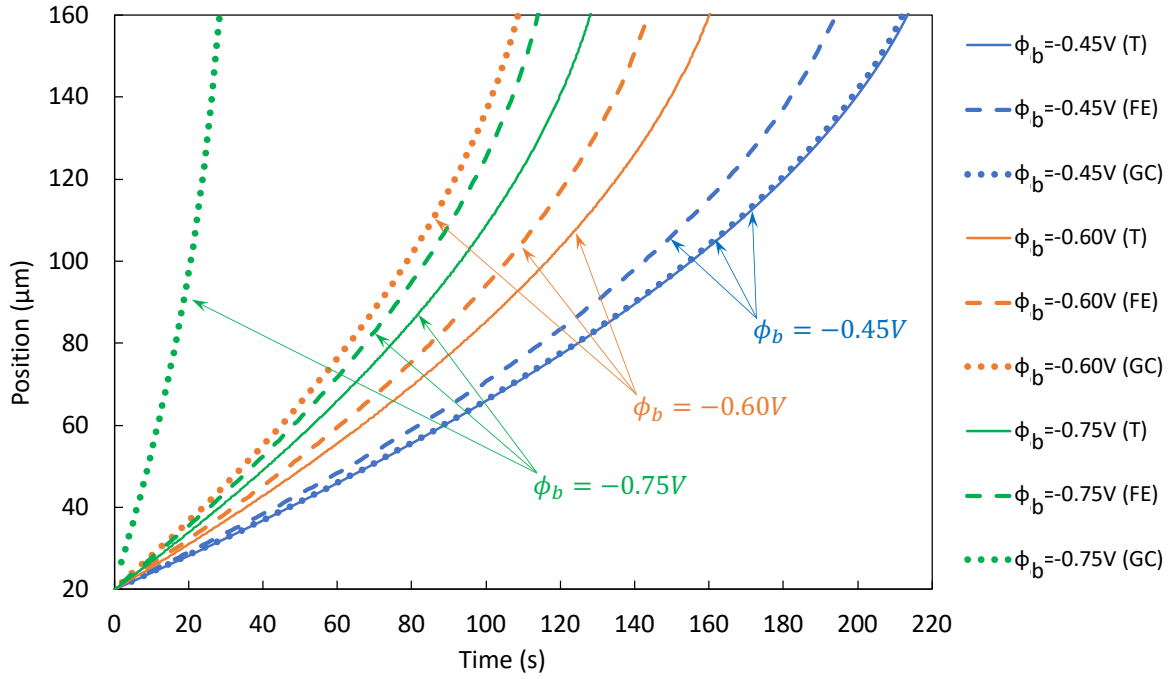
Figure 11 – Interface position vs time for different applied voltages: theoretical rate (T) (30) (solid), simulation results under free energy (dashed), and grand canonical (dotted) approaches.

Figure 11 shows the grand canonical approach (dotted lines) is more sensitive to changes in the applied voltage than the conventional free energy formulation (dashed lines). Taking the position of the electrode after $t = 20\ s$ as an indication of the electrodeposition rate, we obtain relative position differences of 9.75%, 10.9%, and 11.5% for the free energy approach under $-0.45, -0.60$ and $-0.75[V]$, respectively. The grand canonical approach results in larger relative position differences of 1.22%, 51.8%, and over 400% under identical charging conditions. Although we obtain good agreement with the Faradic theory (solid line) using the grand canonical approach to model the lowest applied voltage ($\phi_b = -0.45[V]$), we obtain consistent reaction rates (with comparable position differences under various charging conditions) for the conventional free energy approach ($\tilde{c}_+$).

We select an appropriate phase-field interface thickness (δ_{PF}) by analyzing its effect on the simulated electrodeposition rate, which ultimately determines the evolution time scale (motion) of the electrodeposits. Figure 12 displays a comparative analysis of the simulated electrodeposit position ($\xi = 0.5$) over time for different values of interface thickness ($\delta_{PF} = 1, 5, 10[\mu m]$) under an applied voltage of $\phi_b = -0.45[V]$.
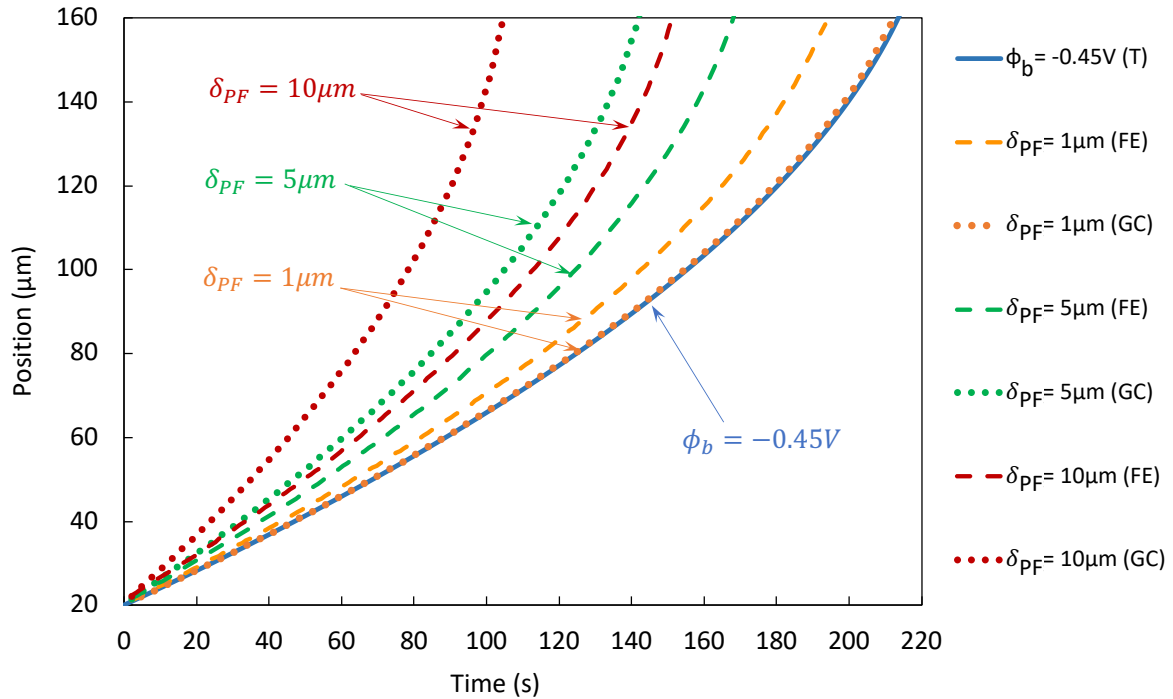
Figure 12 – Interface position vs time for different phase-field interface thickness ($\delta_{PF} = 1, 5, 10[\mu m]$) for applied voltage $\phi_b = -0.45[V]$: theoretical rate (30) (solid), free energy (dashed), and grand canonical (dotted) approaches.

Figure 12 shows that the phase-field interface thickness significantly affects the simulated reaction rates; wider interfaces (larger δ_{PF}) induce extremely fast electrodeposition rates, up to 200% greater than theoretical results. These discrepancies have a physical justification: electrodeposition occurs at the electrode-electrolyte interface; thus, expanding the interface for computational reasons (physical interfaces can be as small as $5[nm]$ [59]) increases the reactive area in the simulation, which induces faster than physical electrodeposition rates. However, as Figure 12 and the position analysis below illustrate, convergent electrodeposition rates (interface-thickness-independent growth) are possible well before reaching the nanometer width interfaces.

Figure 12 includes results for the free energy and grand canonical approaches. Let the electrode position at $t = 100\ s$ be a correlate of the electrodeposition rate, we compute position differences of 10.0%, 29.8%, and 47.2% for the free energy approach using 1, 5, and $10[\mu m]$ interface thicknesses, respectively; alternatively, the grand canonical approach yields relative position differences of 0.43%, 62.6%, and 168% for the same interface thickness values. Therefore, the grand canonical results (dotted lines) are more sensitive to changes in δ_{PF} than those of the conventional free energy formulation (dashed lines).

In short, the grand canonical formulation has greater sensitivity to both the phase-field interface thickness and the applied electric potential value, which practically restricts when the negative applied voltages ($\phi_b < -0.50[V]$) we may simulate in 2D and 3D applications.

Yet, these reaction rates sensitive to negative applied voltages (see Figure 11) guide our detailed analysis of the grand canonical approach using different phase-field interface thicknesses. We did not conduct a similar study of the free energy approach due to its significantly lower sensitivity to the interface thickness and applied voltage as per Figure 11 and Figure 12. We study the interface position plotting it as a function of time for different applied electric potential values in Figure 13 . An interface thickness of $\delta_{PF} = 0.5[\mu m]$ yields a good agreement with the theoretical Faradic rates under $-0.40, -0.45$, and $-0.50[V]$ applied voltages with a spatial resolution of $h = 0.125[\mu m]$ (mesh size) allows for four elements to span the phase-field interface.
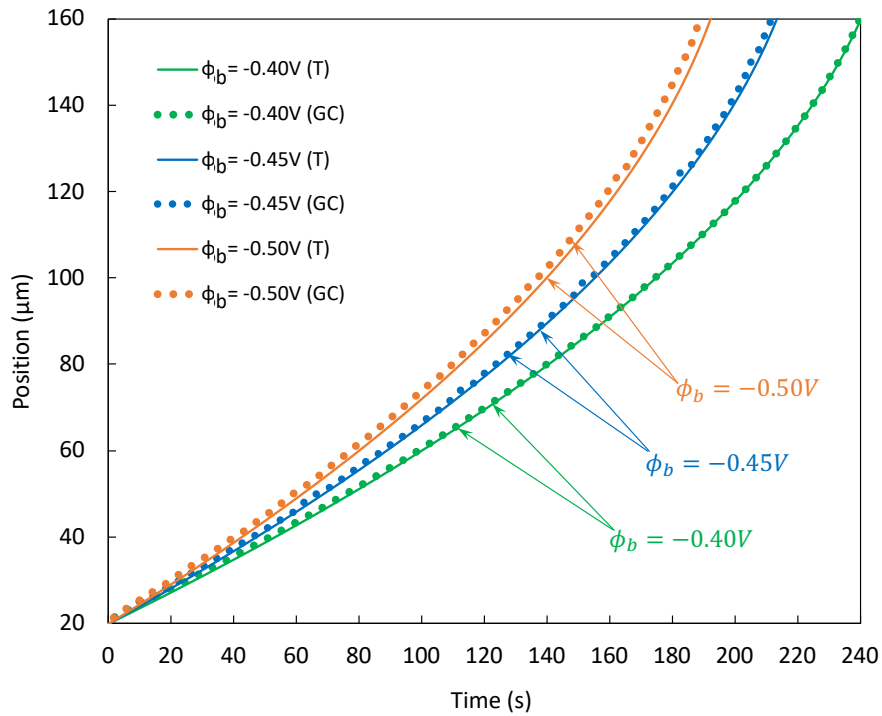

Figure 13 – Interface position vs time for different applied voltages: theoretical electrodeposition rate (30) (solid); simulation results (grand canonical formulation; dotted). Phase-field interface thickness $\delta_{PF} = 0.5[\mu m]$, and $h = 0.125[\mu m]$ mesh size.

Figure 13 shows that the electrodeposition rate accelerates (curved) as the interface approaches the opposite electrode (battery short-circuit condition) [20],[38],[49]. This result agrees with the mathematical model (solid lines), where the deposition rate has a nonlinear relationship. We obtain larger electrodeposition rates under more negative electric potential values (faster battery charge).

We calculate the current density relation to the electrodeposition velocity (ν) using (4). The current density increases as the electrode progresses to the opposite side, producing a nonlinear relationship with the total overpotential (η), as Figure 14 depicts; which satisfies the sharp-interface Butler-Volmer equation: $i = L_\eta \left(e^{-\frac{\alpha n \mathcal{F} \eta}{RT}} - e^{\frac{(1-\alpha) n \mathcal{F} \eta}{RT}} \right)$. Figure 14 shows that as the deposit approaches the opposite electrode, the overpotential slightly increases with time [66], which corresponds to the reaction rate increase due to the Li^+ concentration increase at the electrode-electrolyte interface.
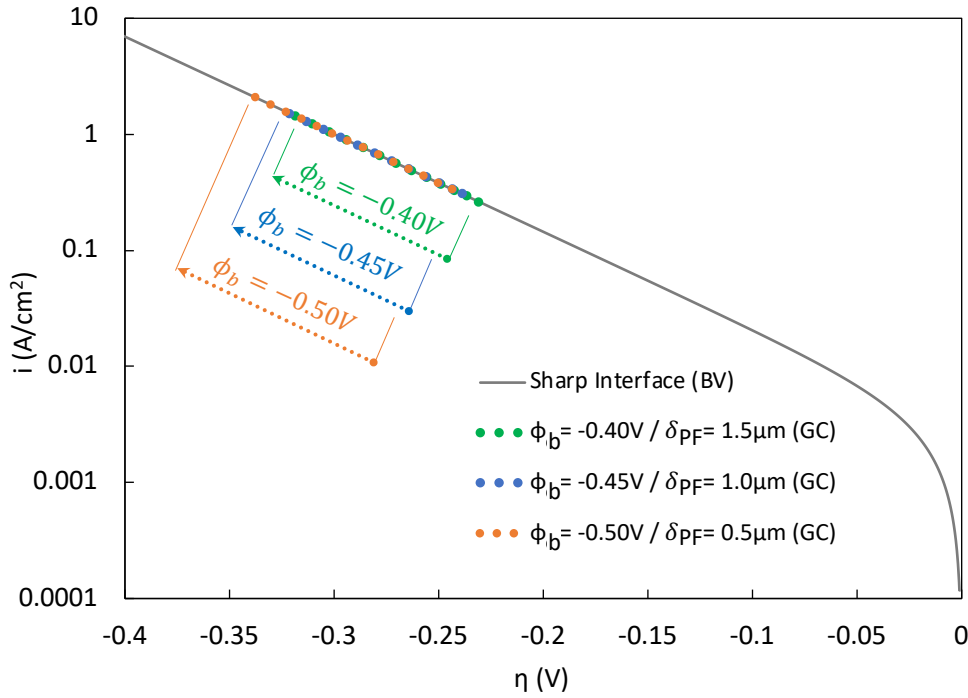
Figure 14 – Comparison of the phase-field model (dotted lines) with the sharp-interface Butler-Volmer equation (solid line) under different electric potential values.

We perform a spatial convergence analysis to verify the convergence rates and quantify the mesh-induced error. We compare flat interface simulation results for different spatial resolutions, $n_x = 400, 800, 1600, 3200, 12800$; (with a domain size of $l_x = 200 [\mu m]$), using a small time-step size ($\Delta t = 6.25 \times 10^{-4} [s]$) to neglect the temporal error, such that $\frac{\Delta t / t_0}{h_{min}/h_0} \ll 1$, where $h_{min} = 0.015625 [\mu m]$ is the finest mesh size.

The position of the electrodeposit interface ($\xi = 0.5$) is the basis of our comparison, since it is the parameter that defines the reaction rate (time-scale) in our simulation. Starting with a $20 \mu m$-thick metal anode, separated from the liquid electrolyte by a $1 [\mu m]$ interface; we compute the final phase-field interface position (electrode position) after $20s$ of simulation under an applied electric potential value of $\phi_b = -0.45 [V]$ (a commonly used electric potential in the literature [23],[24],[26]), using different mesh sizes. The spatial convergence analysis reveals that we obtain grid-independent results

after sufficient mesh refinement (see Figure 15). The agreement between the h = 0.015625[μm] and 0.03125[μm] results (finest and second finest meshes) is of 99.99% and 99.93%, for the free energy formulation and the grand canonical approach, respectively.
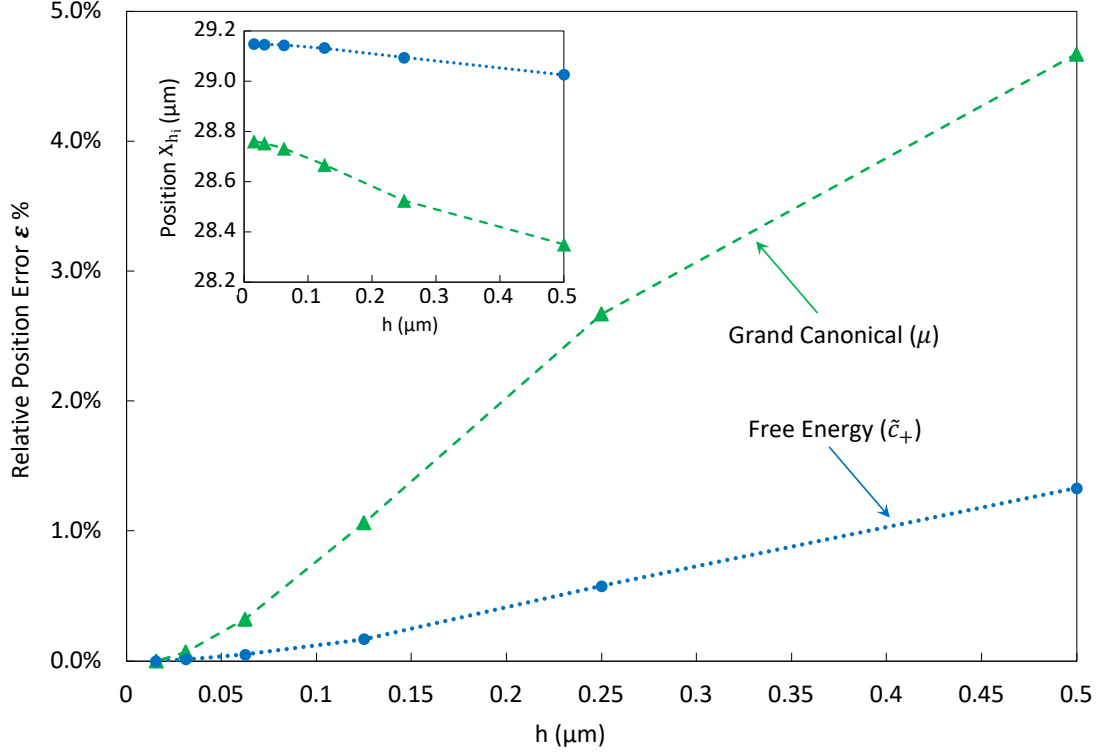

Figure 15 – Relative position error "ε" at $t = 20\ s$ vs mesh sizes h, using free energy (●), and grand canonical (▲) formulations. The inset shows the interface position "X_{h_i}" vs mesh sizes h, using both formulations. Phase-field interface thickness $\delta_{PF} = 1[\mu m]$.

Figure 15 plots the relative error evolution over the mesh size (h). We compute the electrode position errors, relative to the finest mesh resolution (most accurate), as follows: $\varepsilon = \dfrac{X_{h_{min}} - X_{h_i}}{X_{h_{min}} - X_{IC}} \times 100$, where $X_{h_{min}}$, X_{h_i} and X_{IC}, are the electrode position of the finest spatial resolution, the current mesh result, and the electrode's initial thickness (initial position of the phase-field interface), respectively.

Hence, the mesh-induced errors we compute are lower than 5% for the grand canonical approach, and 1.5% for the free energy functional, when utilising the coarsest spatial resolution (h = 0.5[μm], and two linear elements spanning the phase-field interface) to simulate electrodeposition process under $\phi_b = -0.45[V]$. The mesh-induced errors do not significantly affect the electrodeposition rate, compared to the previous ones when varying the phase-field interface thickness.

6. Conclusions

We perform phase-field simulations to describe the flat electrode evolution during metal (lithium) electrodeposition. We solve the coupled equations describing electrochemical interactions during the battery charge cycle using a finite element implementation in an open-source package. We use a sigmoid smoothing function to obtain more robust simulations and significantly reduce the computational cost as an alternative to the widely used polynomial function.

We demonstrate the validity of the current model by comparing the simulation results with theoretical Faradic reactions and the kinetics of the sharp-interface Butler-Volmer model. The comparison analysis between simulations using a phase-field model derived from either a free energy functional or a grand canonical approach allows us to assess each model's sensitivity to the simulation and physical parameters and their robustness. In short, we obtain more consistent results (with comparable position differences under various charging conditions) for the conventional free energy approach. This model shows less sensitivity to changes in the phase-field interface thickness and under different applied voltages than the results obtained using the grand canonical formulation. In particular, we required smaller phase-field interface thicknesses (δ_{PF}), with higher mesh resolution, to capture faster reaction rates under more negative electric potential values using the grand canonical formulation. Consequently, the computational cost significantly increases, making this class of models intractable for applications in two- or three-dimensions under large negative applied voltages involving dendrite growth under fast battery charge.

Additionally, the spatial convergence analysis shows that the mesh-induced errors of up-to 5% for the grand canonical approach, and 1.5% in case of the free energy functional become grid independent (99.99% agreement) after sufficient refinement. Interestingly, these mesh-induced errors have a significantly lower impact in the electrodeposition rate, than those computed by varying the interface thickness (up to 47.2% and 168% relative position differences for the free energy and grand canonical approaches, respectively).

Finally, beyond lithium electrodeposition, this class of phase-field models can appropriately describe other metal deposits in metal-anode batteries, such as zinc anode batteries. The use of one-dimensional simulations as a tool to quantify the resolution requirements of the model under study is an effective strategy, that allows us to set ground rules for further 2D and 3D simulations.

Acknowledgments

7. References

[1]   W. Xu, J. Wang, F. Ding, X. Chen, E. Nasybulin, Y. Zhang, J. -G. Zhang, Lithium metal anodes for rechargeable batteries, Energy Environ. Sci. 7 (2014) 513-537. https://doi.org/10.1039/C3EE40795K.

[2]   J. Fu, Z. P. Cano, M. G. Park, A. Yu, M. Fowler, Z. Chen, Electrically rechargeable zinc–air batteries: progress, challenges, and perspectives, Adv. Mater. 29 (2017) 1604685. https://doi.org/10.1002/adma.201604685.

[3]   Y. Li, J. Lu, Metal–air batteries: will they be the future electrochemical energy storage device of choice? ACS Energy Lett. 2 (2017) 1370–1377. https://doi.org/10.1021/acsenergylett.7b00119.

[4]   B. Liu, J.-G. Zhang, W. Xu, Advancing lithium metal batteries, Joule 2 (2018) 833-845. https://doi.org/10.1016/j.joule.2018.03.008.

[5]   G. Bieker, M. Winter, P. Bieker. Electrochemical in situ Investigations of SEI and dendrite formation on the lithium metal anode, Chem. Phys. 17 (2015) 8670-8679. https://doi.org/10.1039/C4CP05865H.

[6]   B. D. Adams, J. Zheng, X. Ren, W. Xu, J.-G. Zhang, Accurate determination of Coulombic efficiency for lithium metal anodes and lithium metal batteries, Adv. Energy Mater. 8 (2018) 1702097. https://doi.org/10.1002/aenm.201702097.

[7]   D.P. Lv, Y.Y. Shao, T. Lozano, W.D. Bennett, G.L. Graff, B. Polzin, J.G. Zhang, M.H. Engelhard, N.T. Saenz, W.A. Henderson, P. Bhattacharya, J. Liu, J. Xiao, Failure mechanism for fast-charged lithium metal batteries with liquid electrolytes, Adv. Energy Mater. 5 (2014) 1400993. https://doi.org/10.1002/aenm.201400993.

[8]   S. Jiao, J. Zheng, Q. Li, X. Li, M.H. Engelhard, R. Cao, J.-G. Zhang, W. Xu, Behavior of lithium metal anodes under various capacity utilization and high current density in lithium metal batteries, Joule 2 (2018) 110-124. https://doi.org/10.1016/j.joule.2017.10.007.

[9]   M. Rosso, C. Brissot, A. Teyssot, M. Doll´e, L. Sannier, J.-M. Tarascon, R. Bouchet and S. Lascaud, Dendrite short-circuit and fuse effect on Li/polymer/Li cells, Electrochimica Acta, 51 (2006) 5334-5340. 10.1016/j.electacta.2006.02.004.

[10]   P. Bai, J. Z. Guo, M. Wang, A. Kushima, L. Su, J. Li, F. R. Brushett, M.Z. Bazant, Interactions between Lithium Growths and Nanoporous Ceramic Separators, Joule 2 (2018) 2434-2449. https://doi.org/10.1016/j.joule.2018.08.018.

[11]   P. G. Bruce, S. A. Freunberger, L. J. Hardwick, J. -M. Tarascon. Li-O2 and Li-S batteries with high energy storage, Nat. Mater. 11 (2012) 19-29. https://doi.org/10.1038/nmat3191.

[12]   H. Liu, X. -B. Cheng, Z. Jin, R. Zhang, G. Wang, L. -Q. Chen, Q. -B. Liu, J. -Q. Huang, Q. Zhang, Recent advances in understanding dendrite growth on alkali metal anodes, EnergyChem 1 (2019) 100003. https://doi.org/10.1016/j.enchem.2019.100003.

[13] P. Tan, W. Kong, Z. Shao, M. Liu, M. Ni, Advances in modelling and simulation of Li-air batteries, Progress in Energy and Combustion Science 62 (2017) 155-189. https://doi.org/10.1016/j.pecs.2017.06.001.

[14] J. E. Guyer, W. J. Boettinger, J. A. Warren, G. B. McFadden, Phase field modeling of electrochemistry. I. Equilibrium, Phys. Rev. E 69 (2004) 021603. https://doi.org/10.1103/PhysRevE.69.021603.

[15] E. Guyer, W. J. Boettinger, J. A. Warren, G. B. McFadden, Phase field modeling of electrochemistry. II. Kinetics, Phys. Rev. E 69 (2004) 021604. https://doi.org/10.1103/PhysRevE.69.021604.

[16] Y. Shibuta, Y. Okajima, T. Suzuki, Phase-field modelling for electrodeposition process. Sci. Technol. Adv. Mat. 8 (2007) 511-518. https://doi.org/10.1016/j.stam.2007.08.001.

[17] Y. Okajima, Y. Shibuta, T. Suzuki, A phase-field model for electrode reactions with Butler–Volmer kinetics. Comp. Mater. Sci. 50 (2010) 118-124. https://doi.org/10.1016/j.commatsci.2010.07.015.

[18] L. Liang, Y. Qi, F. Xue, S. Bhattacharya, S. J. Harris, L. -Q. Chen, Nonlinear phase-field model for electrode-electrolyte interface evolution, Phys. Rev. E 86 (2012) 051609. https://doi.org/10.1103/PhysRevE.86.051609.

[19] M. Z. Bazant, Theory of Chemical Kinetics and Charge Transfer based on Nonequilibrium Thermodynamics, Acc. Chem. Res. 46 (2013) 1144-1160. https://doi.org/10.1021/ar300145c.

[20] L. Liang, L. Q. Chen, Nonlinear phase field model for electrodeposition in electrochemical systems, Appl. Phys. Lett. 105 (2014) 263903. https://doi.org/10.1063/1.4905341.

[21] D. R. Ely, A. Jana, R. E. Garcia, Phase field kinetics of lithium electrodeposits, J. Power Sources 272 (2014) 581-594. https://doi.org/10.1016/j.jpowsour.2014.08.062.

[22] H. -W. Zhang, Z. Liu, L. Liang, L. Chen, Y. Qi, S. J. Harris, P. Lu, L. -Q. Chen, Understanding and predicting the lithium dendrite formation in li-ion batteries: phase field model, ECS Trans. 61 (2014) 1-9. https://doi.org/10.1149/06108.0001ecst.

[23] L. Chen, H. W. Zhang, L. Y. Liang, Z. Liu, Y. Qi, P. Lu, J. Chen, L. -Q. Chen. Modulation of dendritic patterns during electrodeposition: A nonlinear phase-field model, J. of Power Sources 300 (2015) 376-385. https://doi.org/10.1016/j.jpowsour.2015.09.055.

[24] D. A. Cogswell, Quantitative phase-field modelling of dendritic electrodeposition, Physical Rev. E 92 (2015) 011301R. https://doi.org/10.1103/PhysRevE.92.011301

[25] H. H. Yan, Y. H. Bie, X. Y. Cui, G. P. Xiong, L. Chen, A computational investigation of thermal effect on lithium dendrite growth, Energy Conversion and Management 161 (2018) 193-204. https://doi.org/10.1016/j.enconman.2018.02.002.

[26] Z. Hong, V. Viswanathan, Phase-field simulations of lithium dendrite growth with open-source software, ACS Energy Letters 3, 7 (2018) 1737-1743. https://doi.org/10.1021/acsenergylett.8b01009.

[27] V. Yurkiv, T. Foroozan, A. Ramasubramanian, R. Shahbazian-Yassar, F. Mashayek, Phase-field modelling of solid electrolyte interface (SEI) influence on Li dendritic behaviour, Electrochim Acta 265 (2018) 609-619. https://doi.org/10.1016/j.electacta.2018.01.212.

[28] W. Mu, X. Liu, Z. Wen, L. Liu, Numerical simulation of the factors affecting the growth of lithium dendrites, J. of Energy Storage 26 (2019) 100921. https://doi.org/10.1016/j.est.2019.100921.

[29] Y. Liu, X. Xu, M. Sadd, O. O. Kapitanova, V. A. Krivchenko, J. Ban, J. Wang, X. Jiao, Z. Song, J. Song, Insight into the critical role of exchange current density on electrodeposition behavior of lithium metal, Adv. Sci. 8 (2021) 2003301. https://doi.org/10.1002/advs.202003301.

[30] S. R. de Groot, P. Mazur, Non-equilibrium Thermodynamics, Courier Corporation, New York, 2013.

[31] I. Steinbach, F. Pezzolla, B. Nestler, M. Seeßelberg, R. Prieler, G. J. Schmitz, J. L. Rezende, A phase field concept for multiphase systems, Phys. D 94 (1996) 135-147. https://doi.org/10.1016/0167-2789(95)00298-7.

[32] R. E. Garcia, C. M. Bishop, W. C. Carter, Thermodynamically consistent variational principles with applications to electrically and magnetically active systems, Acta Mater. 52 (2004) 11–21. https://doi.org/10.1016/j.actamat.2003.08.020.

[33] B. C. Han, A. Van der Ven, D. Morgan, G. Ceder, Electrochemical modeling of intercalation processes with phase field models, Electrochim. Acta 49 (2004) 4691-4699. https://doi.org/10.1016/j.electacta.2004.05.024.

[34] S.M. Allen, J. W. Cahn, Ground state structures in ordered binary neighbor interactions, Acta Metall. 20 (1972) 423-433. https://doi.org/10.1016/0001-6160(72)90037-5.

[35] K. J. Vetter, Electrochemical Kinetics: Theoretical and Experimental Aspects, Academic Press, New York, 1967.

[36] A. J. Bard, L. R. Faulkner, Electrochemical methods: Fundamentals and applications, second ed., John Wiley & Sons, Inc, NewYork, 2001.

[37] A. M. Kuznetsov, J. Ulstrup, Electron transfer in chemistry and biology: An introduction to the theory, John Wiley & Sons Ltd, Chichester, U.K., 1999.

[38] K. Nishikawa, T. Mori, T. Nishida, Y. Fukunaka, M. Rosso. Li dendrite growth and Li+ ionic mass transfer phenomenon, Journal of Electroanalytical Chemistry 661 (2011) 84–89. doi:10.1016/j.jelechem.2011.06.035

[39] K. Elder, M. Grant, N. Provatas, J. M. Kosterlitz, Sharp interface limits of phase-field models, Phys. Rev. E 64 (2001) 021604. https://doi.org/10.1103/PhysRevE.64.021604.

[40] J. W. Cahn, J. E. Hilliard, Free energy of a nonuniform system: III. Nucleation in a two‐component incompressible fluid, J. Chem. Phys. 31 (1959) 688-699. https://doi.org/10.1063/1.1730447.

[41] W. J. Boettinger, J. A. Warren, C. Beckermann, A. Karma, Phase-field simulation of solidification, Annual Review of Materials Research 32 (2002) 163-194. https://doi.org/10.1146/annurev.matsci.32.101901.155803.

[42] E. Olsson, G. Kreiss, A conservative level set method for two phase flow, Journal of Computational Physics 210 (2005) 225–246. https://doi.org/10.1016/j.jcp.2005.04.007.

[43] M. Chai, K. Luo, C. Shao, J. Fan, An efficient level set remedy approach for simulations of two-phase flow based on sigmoid function, Chemical Engineering Science 172 (2017) 335-352. https://doi.org/10.1016/j.ces.2017.06.009.

[44] J. -N. Chazalviel, Electrochemical aspects of the generation of ramified metallic electrodeposits, Phys. Rev. A 42 (1990) 7355–7367. https://doi.org/10.1103/PhysRevA.42.7355.

[45] M. Plapp, Unified derivation of phase-field models for alloy solidification from a grand-potential functional, Phys. Rev. E 84 (2011) 031601. https://doi.org/10.1103/PhysRevE.84.031601.

[46] D. A. Cogswell, W. C. Carter, Thermodynamic phase-field model for microstructure with multiple components and phases: The possibility of metastable phases, Phys. Rev. E 83 (2011) 061602. https://doi.org/10.1103/PhysRevE.83.061602.

[47] J. Elezgaray, C. Leger, F. Argoul, Linear stability analysis of unsteady galvanostatic electrodeposition in the two‐dimensional diffusion‐limited regime, J. Electrochem. Soc. 145 (1998) 2016. https://doi.org/10.1149/1.1838592.

[48] B. Trembacki, E. Duoss, G. Oxberry, M. Stadermann, J. Murthy, Mesoscale electrochemical performance simulation of 3D interpenetrating lithium-ion battery electrodes, J. Electrochem. Soc. 166 (2019) A923. https://doi.org/10.1149/2.0031906jes.

[49] C. Monroe, J. Newman, Dendrite growth in lithium/polymer systems: a propagation model for liquid electrolytes under galvanostatic conditions, J. Electrochem. Soc. 150 (2003) A1377-A1384. https://doi.org/10.1149/1.1606686.

[50] L. Vitos, A. Ruban, H. Skriver, J. KollÃar, The surface energy of metals, Surf. Sci. 411 (1998) 186-202. https://doi.org/10.1016/S0039-6028(98)00363-X.

[51] R. Tran, Z. Xu, B. Radhakrishnan, D. Winston, W. Sun, K. A. Persson, S. Ping Ong, Surface energies of elemental crystals, Scientific Data 3 (2016) 160080. https://doi.org/10.1038/sdata.2016.80.

[52] L. O. Valøen, J. N. Reimers, Transport properties of LiPF6-based li-ion battery electrolytes, J. Electrochem. Soc. 152 (2005) A882-A891. https://doi.org/10.1149/1.1872737.

[53] M. S. Alnaes, J. Blechta, J. Hake, A. Johansson, B. Kehlet, A. Logg, C. Richardson, J. Ring, M. E. Rognes, G. N. Wells, The FEniCS project version 1.5, Archive of Numerical Software 3, 2015.

[54] A. Logg, K.-A. Mardal, G. N. Wells, Automated solution of differential equations by the finite element method: The FEniCS book, Springer Science & Business Media, Berlin, 2012.

[55] H. -l. Liao, B. Ji, L. Zhang. An adaptive BDF2 implicit time-stepping method for the phase field crystal model. IMA Journal of Numerical Analysis 42 (2022) 649-679. https://doi.org/10.1093/imanum/draa075.

[56] Hughes, Thomas JR. The finite element method: linear static and dynamic finite element analysis, Courier Corporation, New York, 2012.

[57] D. Pardo, P. Matuszyk, V. Puzyrev, C. Torres-Verdin, M. Nam, V. M. Calo, Modeling of resistivity and acoustic borehole logging measurements using finite element methods, Elsevier, 2021.

[58] S. Balay, S. Abhyankar, M. Adams, J. Brown, P. Brune, K. Buschelman, L. Dalcin, A. Dener, V. Eijkhout, W. Gropp, D. Karpeyev, D. Kaushik, M. Knepley, D. Day, L. Curfman McInnes, R. Mills, T. Munson, K. Rupp, P. Sanan, B. Smith, S. Zampini, H. Zhang, H. Zhang, PETSc Users Manual, ANL-95/11 Revision 3.15 (2021) 170061. https://doi.org/10.2172/1814627.

[59] K. -I. Morigaki, Analysis of the interface between lithium and organic electrolyte solution, Journal of Power Sources 104 (2002) 13-23. https://doi.org/10.1016/S0378-7753(01)00871-0.

[60] A. Karma, Phase-field formulation for quantitative modeling of alloy solidification, Phys. Rev. Lett. 87 (2001) 115701. https://doi.org/10.1103/PhysRevLett.87.115701.

[61] B. Echebarria, R. Folch, A. Karma, M. Plapp, Quantitative phase-field model of alloy solidification, Phys. Rev. E 70 (2004) 061604. https://doi.org/10.1103/PhysRevE.70.061604.

[62] Y. Zhao, B. Zhang, W. Chen, H. Wang, M. Wang, H. Hou. Simulation for the influence of interface thickness on the dendritic growth of nickel-copper alloy by a phase-field method. ES Mater. Manuf. 2 (2018) 45-50. http://dx.doi.org/10.30919/esmm5f135.

[63] N. A. Labanda, L. Espath, V. M. Calo, A spatio-temporal adaptive phase-field fracture method. arXiv:2110.03305 (2021).

[64] E. Hairer, G. Wanner. Solving ordinary differential equations II: stiff and differential-algebraic problems, Springer, Berlin, 2010.

[65] R. Akolkar, Mathematical model of the dendritic growth during lithium electrodeposition, Journal of Power Sources, 232 (2013) 23-28. https://doi.org/10.1016/j.jpowsour.2013.01.014.

[66] V. R. Subramanian, V. Boovaragavan, V. Ramadesigan, M. Arabandi, Mathematical Model Reformulation for Lithium-Ion Battery Simulations: Galvanostatic Boundary Conditions, J. Electrochem. Soc. 156 (2009) A260. https://doi.org/10.1149/1.3065083.